

Through-Thickness Modelling of Metal Rolling using Multiple-Scales Asymptotics

Mozhdeh Erfanian¹, Edward J. Brambley^{1,2}, Francis Flanagan³,
Doireann O’Kiely³ & Alison N. O’Connor^{4,5}

¹Mathematics Institute, University of Warwick, Coventry, UK

²WMG, University of Warwick, Coventry, UK

³MACSI, Department of Mathematics & Statistics, University of Limerick, Ireland

⁴ Computer Science and Information Systems (CSIS), University of Limerick, Ireland

⁵ Lero, The Science Foundation Ireland Centre for Software Research, University of Limerick, Ireland

Abstract

A new semi-analytic model of the metal rolling process is presented and validated against finite element simulations. The model generalises the classical slab method of modelling cold rolling, and for the first time, is able to predict the through-thickness stress and strain oscillations present in long thin roll gaps. The model is based on the asymptotic method of multiple scales, with the systematic assumptions of a long thin roll gap and a comparably small Coulomb friction coefficient. The leading-order solution varies only on a long length scale corresponding to the roll-gap length and matches with slab methods. The next-order correction varies on both this long length scale and a short length scale associated with the workpiece thickness, and reveals rapid stress and strain oscillation both in the rolling direction and through the thickness. For this initial derivation, the model assumes a rigid perfectly-plastic material behaviour. Despite these strong assumptions, this model compares well with finite element simulations that employ more realistic material behaviour (including elasticity and strain hardening). These assumptions facilitate the simplest possible model to provide a foundational understanding of the complex through-thickness behaviour observed in the finite element simulations, while requiring an order of only seconds to compute. MATLAB code for evaluating the model is provided in the supplementary material.

Keywords: mathematical modelling; plastic deformation; multiple-scales asymptotics; cold rolling; quick-to-compute; through-thickness.

1 Introduction

Rolling, depicted in Figure 1, is the process of reducing the thickness of a workpiece by passing it between two work rolls. It is a major industrial process in metal manufacturing, with over 99% of cast steel and two-thirds of wrought aluminium produced being rolled [1, pp. 54–55]. The rolling process is usually repeated for several passes until the desired thickness is achieved, either by moving the workpiece backwards and forward through the same pair of rolls, or by having several roll stands in tandem which the workpiece passes through in sequence. Usually either one, or both, of the work rolls is mechanically driven, and the workpiece is pulled through the roll gap by friction between the workpiece and the rolls. In addition to altering the thickness, cold rolling alters the material’s physical properties, a modification which is arguably of more importance for the final product [2].

The modelling of strip rolling is highly significant to industry as a potential means of reducing material waste, and driving towards carbon neutrality and sustainability [3]. Modern set-up and control algorithms for rolling mills aspire to go beyond controlling only geometry, utilizing models which, in addition to predicting how key quantities such as roll load and torque depend on the rolling parameters, also include basic microstructural modelling [4]. Finite Element (FE) simulations are considered the ‘gold standard’ method of analysing rolling processes [5–7]. However, despite their accuracy, the long computational time of FE simulations prohibits their deployment in real-time applications. Moreover, FE simulations of rolling have shown to not include sufficient through-thickness resolution to model fine through-thickness variations until recently [8], which is a pre-requisite for accurately modelling microstructural development [9]. These limitations motivate the exploration of fast models that can support real-time process control while including through-thickness variation. Fast models are often based on equations drawn from physical principles, with some simplifying assumptions that enable analytical or semi-analytical solution.

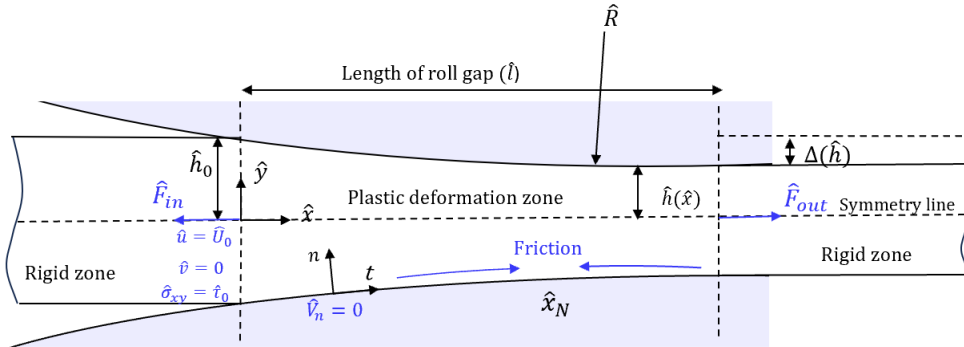


Figure 1: Schematic diagram of symmetric rolling with the domain of interest and the boundary conditions. The sheet, which is wide in the direction into the page, enters the rollgap between the two rolls from the left and exits as a thinner sheet to the right.

Historically, fast rolling models aimed to predict only roll force and roll torque in order to enable gauge control [10, 11]. These fast models were established from the equilibrium of forces acting on each vertical slab of material in the zone of deformation; a method commonly known as the ‘slab method’. Slab models were subsequently improved by including more complex material models and accounting for roll elasticity, by adjusting the roll shape [e.g. 12, 13]. However, one consequence of the slab method is the inability to predict through-thickness variation; in effect, the slab method involves an implicit assumption that the deformation is homogeneous through-thickness.

Orowan [14] was among the first to discard the assumption of homogeneous through-thickness deformation by modifying the shape of the slab to a thin segment bounded by circular arcs. The Nadai [15] solution is then applied to this new geometry, which enabled the inclusion of through-thickness shear in the model. This was followed by a series of developments [16–18] which extended Orowan’s original work to incorporate tensions or to simplify the calculation process with additional assumptions.

Models originating from a slab method predict a single pressure peak throughout the roll gap. However, MacGregor and Palme [19] experimentally demonstrated a wave-like roll pressure with multiple peaks. Similarly, using the method of sliplines, for a sheet with comparable half thickness and length, Firbank and Lancaster [20] also found two pressure peaks with a marked drop in pressure between them. This finding set the stage for further study where Al-Salehi, Firbank, and Lancaster [21] conducted a series of experiments with different materials and aspect ratios and measured multiple pressure peaks. This oscillatory pattern was later verified using FE analyses [8, 22–25], which demonstrates that the wave-like roll pressure observed is a consequence of a complicated through-thickness behaviour. These findings imply that slab models, due to their simplified through-thickness assumptions, can not accurately model the wave-like oscillations noted to occur in both experiments and FE simulations. It is clear that the oscillatory patterns are critical in understanding how the mechanical material behaviour and the cold rolling process parameters interact. Without accurately capturing these patterns, the impact of any real-time monitoring algorithms will be severely limited.

A more rigorous mathematical framework for deriving fast approximate models is asymptotic analysis. Asymptotics utilises systematic assumptions of scale, as opposed to simplifications through ad-hoc assumptions of unknown error and limitation [26]. This approach is especially effective in situations where parameters are not of the same magnitude (i.e., one parameter is notably smaller compared to the others). As such, asymptotics has found successful application in the modelling of rolling, where the presence of a small parameter is readily identifiable. Smet and Johnson [27] developed the first asymptotic formulation of the sheet metal rolling process and accounted for through-thickness variation in the flow and the inhomogeneous work hardening it caused. This technique has subsequently been used in other studies with different perturbation parameters, such as the ratio of yield stress to maximum pressure by Domanti and McElwain [28], the ratio of entry-gauge thickness to roll-bite length initially by Johnson and Smelser [29] and more recently for sandwich rolling [30] and asymmetric clad-sheet rolling [26]. Although asymptotic models incorporate the effect of shear evolution through the thickness, they are often only validated at the workpiece surface, which does not necessarily represent the heterogeneity of through-thickness distribution [27–29].

FE simulations can be used to validate theoretical models. In fact, validation via FE simulation

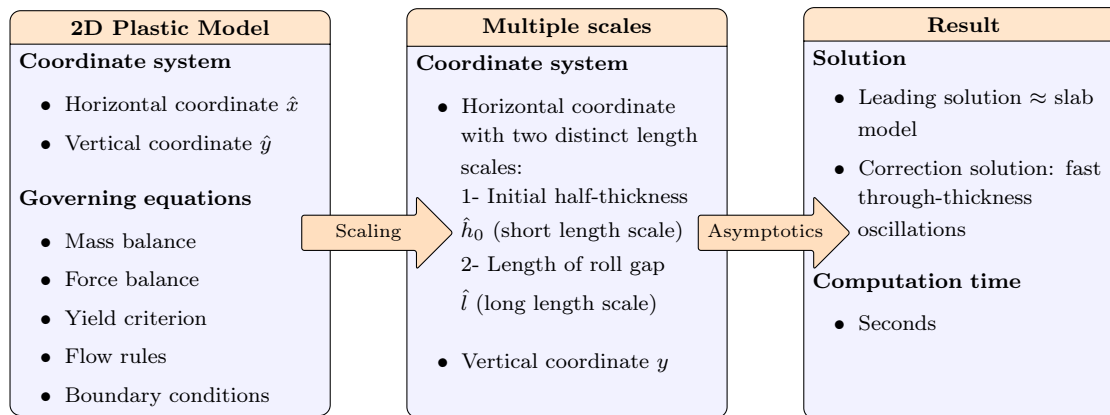


Figure 2: Outline of the development of the asymptotic multiple-scales model in section 2, 3, and 4.

is preferable to experimental methods given the difficulty and expense in capturing through-thickness stress and strain heterogeneity. However, comparisons of theoretical models with FE simulations are infrequent in the literature. Minton [31] compared his asymptotic models for different rolling processes with results from the commercial FE package ABAQUS [32]. He reported through-thickness oscillatory patterns in the shear stress fields for all FE simulations of asymmetric, thick sheet and clad-sheet rolling. Through a careful study, he demonstrated that the oscillatory pattern is pervasive in rolling, regardless of the material’s rigidity or work hardening properties, the type of solver used (implicit or explicit), and whether the workpiece is three-dimensional or exhibits plane strain. These oscillatory patterns, however, are not captured in his asymptotic models [26, 30].

Careful FE simulations [8, 25, 31] show that the through-thickness pattern oscillates rapidly in the axial direction on the length scale of the sheet thickness; a length scale which previous asymptotic analyses have ignored as small compared with the overall deformation. The existence of effects on two different length scales in the same axial direction requires a different type of asymptotic analysis, termed multiple scales [33], in which a fast scale provides rapid small variations about a solution which slowly evolves on the slow scale. The slowly varying solution is sometimes referred to as a slow manifold, invariant manifold, or centre manifold, and is a more general concept that is not unique to asymptotics [see, e.g. 34]. These techniques of a fast variation about a slowly-varying solution have been applied to elastic beams [35], lubricating flows [36], and acoustics [37], but to our knowledge have not previously been used in the modelling of rolling.

To predict and manage material microstructures during forming processes, a description of the through-thickness shear evolution is essential. Through this literature exploration, it is evident that fast rolling models, with sufficient through-thickness resolution, validated against a reliable source, is an ongoing challenge. Building upon this inspiration, the current work develops an asymptotic model capable of predicting inhomogeneous through-thickness shear effects. Furthermore, our results are validated against an implicit FE simulation using ABAQUS [32]. Our emphasis is on developing the simplest possible asymptotic model to provide a foundational understanding of the principles underlying through-thickness variation during the rolling process. In doing so, we neglect many factors that complicate the dynamics of rolling in reality, including anisotropic elasto-plastic material deformation in the workpiece, roll flattening, and varying friction coefficients on the rolls. Nonetheless, the outcomes obtained are by no means trivial, explaining the multiple pressure peaks and the seemingly complex FE observations while requiring an order of seconds to compute. The use of small parameters in the model is justified by the range of parameters involved in industrial practice. In a typical sheet-rolling schedule, the sheet passes through a sequence of roll stands with the roll-gap thickness:length ratio typically varying between 1:10 and 3:10. The effective Coulomb friction coefficient typically lies in the range of 0.05–0.2, depending on the roll characteristics and presence of lubricant [28]. Consequently, we may assume that both the roll-gap thickness-to-length ratio and the friction coefficient are small, although due to the asymptotic framework, they are not neglected entirely.

The paper is structured as shown schematically in Figure 2; the governing equations and modelling assumptions are presented in Section 2 where all the parameters are non-dimensionalised and the equations are scaled by two length scales using the method of multiple scales. The equations are then solved in Section 3 by performing asymptotic analysis on the governing equations, and the solution is provided

at different asymptotic orders. The assumption of a perfect plastic material allows for solving the stress field independent of strain, and therefore the solutions for the stress and velocity fields are provided in separate subsections 3.1 and 3.2. In Section 4, the solutions are summarised and the computation methods are explained for stress and velocities in sections 4.1 and 4.2, respectively. We have carefully constructed these sections so that readers who are not interested in the details of the multiple-scales analysis can skip Section 3 completely, and find the key outputs of the analysis and how to compute them in Section 4. Finally, these outputs are validated against FE simulation results for a range of parameters in Section 5, including against FE simulations using realistic material hardening parameters in Section 5.3. Implications of this work, and possibilities for future research, are then discussed in Section 6.

2 Governing Equations

A schematic of the rolling problem under consideration is presented in Figure 1, with the control volume, boundary conditions and coordinate systems all illustrated. We initially work with dimensional variables, denoted with a hat, before non-dimensionalising in Section 2.1. The lateral spread in the third dimension is minimal away from the workpiece edges for sufficiently wide workpieces (width-to-thickness ratio >10 [2]), reducing the problem to a two-dimensional plane strain problem in coordinates \hat{x} and \hat{y} [28]. Since the system considered here is symmetric about the sheet centre, we need only consider the upper half of the sheet shown in Figure 1. The rolls are held at a fixed separation that is less than the initial thickness of the sheet and the top roll rotates anti-clockwise so that the sheet moves in the positive \hat{x} -direction. The sheet has an initial thickness $2\hat{h}_0$ and the reduction r reduces this thickness by $r\hat{h}_0$ top and bottom, giving a final thickness of $2(1-r)\hat{h}_0$. Attention is restricted to the region $0 \leq \hat{x} \leq \hat{\ell}$ in which the sheet is in contact with the rolls, referred to as the roll gap, where $\hat{\ell} = \sqrt{2r\hat{h}_0\hat{R} - r^2\hat{h}_0^2}$ is the length of the roll gap in terms of the roll radius \hat{R} . Typically, unless the reduction is very small, $\hat{\ell}$ is much larger than \hat{h}_0 , giving a long thin roll gap.

The workpiece material is assumed to be perfectly plastic (i.e. non-hardening), and elastic effects are ignored in both the workpiece and the rolls. This results in the same set of equations used by Minton et al. [26], although here a different solution method is followed. The unknown normal and shear Cauchy stresses, $\hat{\sigma}_{xx}$, $\hat{\sigma}_{yy}$ and $\hat{\sigma}_{xy}$, follow the von Mises yield criterion and momentum conservation (neglecting inertia),

$$\frac{1}{4}(\hat{\sigma}_{xx} - \hat{\sigma}_{yy})^2 + \hat{\sigma}_{xy}^2 = \hat{\kappa}^2, \quad \frac{\partial \hat{\sigma}_{xx}}{\partial \hat{x}} + \frac{\partial \hat{\sigma}_{xy}}{\partial \hat{y}} = 0 \quad \text{and} \quad \frac{\partial \hat{\sigma}_{xy}}{\partial \hat{x}} + \frac{\partial \hat{\sigma}_{yy}}{\partial \hat{y}} = 0, \quad (1)$$

where $\hat{\kappa}$ is the known yield stress in shear, which relates to the yield stress in tension, \hat{Y} , by $\hat{Y} = \sqrt{3}\hat{\kappa}$. The interface between the workpiece and the rolls is assumed to be slipping throughout the roll gap and is modelled using Coulomb friction as $\mathbf{t} \cdot \hat{\boldsymbol{\sigma}} \cdot \mathbf{n} = \pm\mu\mathbf{n} \cdot \hat{\boldsymbol{\sigma}} \cdot \mathbf{n}$, where \mathbf{n} and \mathbf{t} are the unit normal and unit tangent vectors to the surface respectively. The friction coefficient μ is also assumed to be a known constant. The \pm sign accounts for the direction of slip of the workpiece over the rolls, as shown in Figure 1. Since the workpiece enters the roll gap slowly and exits it faster while the rolls rotate at a constant rate, there exists a position, \hat{x}_N , referred to as the neutral point, where the speed of the workpiece surface is the same as that of the rolls.

Acquiring a better understanding of the problem's kinematics is advantageous in interpreting how the material deforms and undergoes strain, which in turn affects the microstructure. The unknown horizontal (rolling direction) and vertical (through-thickness direction) velocities \hat{u} and \hat{v} , and the plastic multiplier $\hat{\lambda}$, satisfy mass conservation and flow rule equations,

$$\frac{\partial \hat{u}}{\partial \hat{x}} + \frac{\partial \hat{v}}{\partial \hat{y}} = 0, \quad \frac{\partial \hat{u}}{\partial \hat{x}} = \frac{1}{2}\hat{\lambda}(\hat{\sigma}_{xx} - \hat{\sigma}_{yy}), \quad \text{and} \quad \frac{1}{2}\left(\frac{\partial \hat{u}}{\partial \hat{y}} + \frac{\partial \hat{v}}{\partial \hat{x}}\right) = \hat{\lambda}\hat{\sigma}_{xy}. \quad (2)$$

(Note that we use \hat{u} for the horizontal velocity, and not for the displacement; in what follows, we will always be dealing with velocities and never with displacements.) The velocity on the roll surfaces is restricted by the no-penetration condition $\hat{V}_n = 0$, where \hat{V}_n is the normal component of sheet velocity.

The boundary conditions at the entrance and exits are a given force per unit width, $\hat{F}_{\text{in/out}}$, at each end of the roll gap, and the presumed shear stress distribution, $\hat{\tau}_0$, at the entrance. Velocity constraints are also applied at the entrance, where a zero vertical velocity and a constant horizontal velocity \hat{U}_0 are assumed. Finally, the model is closed by applying symmetry about the centre line $\hat{y} = 0$.

It is sometimes convenient to write the Cauchy stresses $\hat{\sigma}_{ij}$ in terms of the deviatoric stresses \hat{s}_{ij} and the hydrostatic pressure \hat{p} , where, in plane strain,

$$\hat{\sigma}_{ij} = \hat{s}_{ij} - \hat{p}\delta_{ij} \quad \text{and} \quad -\hat{p} = \frac{1}{2}(\hat{\sigma}_{xx} + \hat{\sigma}_{yy}). \quad (3)$$

Here, compressive stresses are negative, hence the negative sign in the definition of hydrostatic pressure.

It will also be useful in the analysis below to use a thickness-averaged description of mass conservation, describing the mass balance in each through-thickness slice. Integrating the mass conservation law in (2) from $\hat{y} = -\hat{h}$ to $\hat{y} = +\hat{h}$ and applying the no-penetration rule $\hat{v} = \hat{u}d\hat{h}/d\hat{x}$ yields

$$\int_{-\hat{h}(\hat{x})}^{\hat{h}(\hat{x})} \hat{u} \, d\hat{y} = 2\hat{U}_0\hat{h}_0. \quad (4)$$

2.1 Scaling and non-dimensionalisation

An important part of the analysis here comes from the exploitation of small dimensionless parameters. We therefore rescale the variables in terms of the dimensional scales relevant to the problem; hats on variables denote dimensional quantities, and unhatted variables are their dimensionless equivalents. In what follows, distances are measured in multiples of the workpiece initial half-thickness \hat{h}_0 , shown in Figure 1, so that the horizontal distance from the roll-gap entrance is $\hat{x} = \hat{h}_0x$ and vertical distance from the workpiece centre line is $\hat{y} = \hat{h}_0y$. The upper roll surface is located at $\hat{y} = \hat{h}(\hat{x}) = \hat{h}_0h(x)$. Therefore, in dimensionless terms, the vertical gap between the rolls is from $y = -h(x)$ to $y = h(x)$ owing to symmetry, and the roll gap extends horizontally from $x = 0$ to $x = 1/\delta$, where $\delta = \hat{h}_0/\hat{\ell}$ is the reciprocal of the roll-gap aspect ratio, and so is typically small. All stresses are non-dimensionalised with respect to the yield stress $\hat{\kappa}$, and correspondingly, the entrance and exit tensions per unit width $\hat{F}_{\text{in/out}}$ are non-dimensionalised with $\hat{\kappa}\hat{h}_0$. Similar to Minton [31], velocities are scaled by the upstream workpiece horizontal velocity $\hat{U}_0 = \hat{u}(0, \hat{y})$. Finally, the plastic parameter, $\hat{\lambda}$, is non-dimensionalised according to its units and the preceding non-dimensionalisations with $\hat{U}_0/(\hat{h}_0\hat{\kappa})$.

In this study, small values of δ (corresponding to narrow roll gaps) are of interest, which is justified for cold rolling processes and is commonly assumed in many asymptotic models for cold rolling [26, 28, 38]. Another small parameter in this model is the friction coefficient, μ , which is typically of the same order of magnitude as δ . Following previous asymptotic studies [26, 30, 38], we formally encoded this here by setting $\mu = \delta\beta$, where β may be thought of as the normalised friction coefficient.

2.1.1 Multiple scales

The horizontal coordinate \hat{x} was scaled above with a small length scale \hat{h}_0 , yielding a rapidly-varying dimensionless horizontal variable x . While this short scale will be found later to indeed be important, it contrasts with results from classical slab methods and FE analyses which suggest the pressure on the roll surface slowly increases and then decreases over the length of the roll gap, $\hat{\ell}$, forming a profile known as the ‘‘pressure hill’’. This indicates a dependence of the result on large length scale $\hat{\ell}$ as well as on the short length scale \hat{h}_0 . We therefore incorporate both length scales into the mathematical model using the method of multiple scales [33].

We define a large-scale dimensionless horizontal coordinate $z = \delta x$ (equivalently, $z = \hat{x}/\hat{\ell}$), such that the roll-gap entrance is at $z = 0$ and the exit is at $z = 1$. The shape of the rolls necessarily varies on this length scale only, and so $h(x)$ is now written $h(x) = h(z)$ to demonstrate this dependence. In order to capture small-scale behaviour, rather than using x directly, it turns out to be appropriate to use a WKB variable, n , which measures distance through the roll gap based on the number of roll-gap-thicknesses from the entrance. Since the roll-gap thickness is varying, so too is the rate of variation of n , and we therefore have that

$$\frac{d\hat{x}}{dn} = \hat{h}(\hat{x}) \quad \Rightarrow \quad n = \int_0^{\hat{x}} \frac{d\hat{X}}{\hat{h}(\hat{X})} = \int_0^z \frac{dZ}{\delta h(Z)}. \quad (5)$$

We can now think of the roll gap being measured in terms of two lengths; one extending from $n = 0$ to $n \sim O(1/\delta)$, and the other, from $z = 0$ to $z = 1$. If the solution $\phi(x, y)$, representing any of the mentioned variables, is assumed to depend on the short length scale through n and the long length scale through z , then formally $\phi(x, y) = \phi(n, z, y)$, and

$$\frac{\partial\phi}{\partial x} = \frac{1}{h} \frac{\partial\phi}{\partial n} + \delta \frac{\partial\phi}{\partial z}. \quad (6)$$

To summarise, non-dimensionalised horizontal distances x , n and z are defined as

$$x = \hat{x}/\hat{h}_0 \quad (7a)$$

$$n = \int_0^{\hat{x}} \frac{d\hat{X}}{\hat{h}(\hat{X})} \quad \text{— the rapidly-changing variable} \quad (7b)$$

$$z = \hat{x}/\hat{\ell} = \delta x \quad \text{— the slowly-changing variable.} \quad (7c)$$

The dependence of results on both the large and small length scales was missing in the previous asymptotic study of rolling by Minton et al. [26], who assumed all horizontal behaviour was only on the large length scale, and this will be shown to have led to inaccurate results.

2.1.2 Non-dimensional governing equations

Based on the non-dimensionalisation and the multiple-scales variables described above, the governing equations (1) and (2) become

$$\frac{1}{4}(\sigma_{xx} - \sigma_{yy})^2 + \sigma_{xy}^2 = 1, \quad (8a)$$

$$\frac{1}{h(z)} \frac{\partial\sigma_{xx}}{\partial n} + \delta \frac{\partial\sigma_{xx}}{\partial z} + \frac{\partial\sigma_{xy}}{\partial y} = 0, \quad (8b)$$

$$\frac{\partial\sigma_{yy}}{\partial y} + \frac{1}{h(z)} \frac{\partial\sigma_{xy}}{\partial n} + \delta \frac{\partial\sigma_{xy}}{\partial z} = 0, \quad (8c)$$

$$\frac{1}{h(z)} \frac{\partial u}{\partial n} + \delta \frac{\partial u}{\partial z} + \frac{\partial v}{\partial y} = 0, \quad (8d)$$

$$\frac{1}{h(z)} \frac{\partial u}{\partial n} + \delta \frac{\partial u}{\partial z} = \frac{1}{2} \lambda(\sigma_{xx} - \sigma_{yy}), \quad (8e)$$

$$\frac{\partial u}{\partial y} + \frac{1}{h(z)} \frac{\partial v}{\partial n} + \delta \frac{\partial v}{\partial z} = 2\lambda\sigma_{xy}. \quad (8f)$$

The Coulomb friction condition applied on the roll surface $y = h(z)$ is expressed as

$$\delta \frac{dh}{dz} (\sigma_{yy} - \sigma_{xx}) + \left(1 - \delta^2 \left(\frac{dh}{dz}\right)^2\right) \sigma_{xy} = \mp \delta \beta \left(\sigma_{yy} - 2\delta \frac{dh}{dz} \sigma_{xy} + \delta^2 \left(\frac{dh}{dz}\right)^2 \sigma_{xx} \right), \quad (9)$$

where $\mp = \text{sgn}(x - x_N)$ gives the correct direction of the friction force before and after the neutral point x_N . The latter convention is kept for the rest of the paper, thus the $-$ ve sign in \mp refers to the zone before the neutral point ($\hat{x} < \hat{x}_N$), and the $+$ sign refers to the zone after the neutral point ($\hat{x} > \hat{x}_N$). In equation (9), the gradient of thickness is written as $dh/dx = \delta dh/dz$, indicating, firstly, that the shape of the rolls, h , necessarily varies on the large length scale z , and correspondingly, that the rate of change in thickness is small which is the result of a long and thin roll gap.

Assuming non-dimensionalised tensions per unit width $F_{\text{in/out}}$ are applied at the entrance and exit, the horizontal stress must satisfy

$$F_{\text{in/out}} = \int_{-h_{\text{in/out}}}^{h_{\text{in/out}}} \sigma_{xx}(z = n = 0) dy, \quad (10)$$

where $h_{\text{in}} = 1$ by our non-dimensionalization, and h_{out} is half of the final thickness imposed by the rolls. Velocity and shear stress are also assumed to be prescribed at the entrance as,

$$u(z = n = 0) = 1, \quad v(z = n = 0) = 0, \quad \text{and} \quad \sigma_{xy}(z = n = 0) = \delta\tau_0, \quad (11)$$

where we assume that the imposed shear stress at the entrance is $O(\delta)$, and so $\tau_0 = \hat{\tau}_0/(\delta\hat{\kappa})$ is the nondimensionalisation used. This will turn out below to be the correct number of boundary conditions to apply, as will be seen once we have derived the solution.

The no-flux constraint on the roll surface $y = h(z)$ leads to

$$v = \delta \frac{dh}{dz} u. \quad (12)$$

Finally, symmetry about the centre line at $y = 0$ is applied,

$$\sigma_{xy}(y = 0) = 0 \quad \text{and} \quad v(y = 0) = 0. \quad (13)$$

The averaged mass balance (4) becomes

$$\int_{-h(z)}^{h(z)} u \, dy = 2. \quad (14)$$

Our next step is to take the model written in terms of the two longitudinal length scales (8)-(13), and analyse it using asymptotic analysis. This procedure is outlined in Section 3 below. We note that the mathematical description of the rolling system does temporarily become more complicated as a result of the multiple length scales and asymptotic analysis, but upon completion of the analysis will yield a simpler and faster-to-compute model. Readers uninterested in the technical details may safely skip the next section, and refer directly to Section 4 where the outputs of the model are summarised before being compared to FE simulations in Section 5.

3 Asymptotic Solution

This section details the solution of equations (8)-(13) using an asymptotic expansion in powers of the small parameter δ . The resulting equations are summarised at the beginning of Section 4, which then goes on to describe their practical use. Readers uninterested in the technical details in this section may therefore safely skip forward to Section 4.

In order to solve equations (8)-(13), the stress components, velocity components, and plastic parameter are expanded as asymptotic series in the small parameter δ ,

$$\phi = \phi^{(0)}(z, y) + \delta \phi^{(1)}(n, z, y) + \delta^2 \phi^{(2)}(n, z, y) + O(\delta^3), \quad (15)$$

where ϕ represents any of the mentioned variables. Under the assumption that δ is small, each power of δ represents a small correction to the terms preceding it. Note that the leading-order terms in all variables are set to be independent of n , which is in line with the slab method and will be justified a posteriori.

We now proceed to solve the problem presented in Section 2.1.2 by substituting the expansion (15) into the non-dimensionalised governing equations (8) and boundary conditions (9) to (13) and collecting terms with like powers of δ . Anticipating that the stress is independent of velocity, we first derive a solution for the stress components, before returning to the velocities in Section 3.2.

3.1 Solving for the Stresses

By asymptotically expanding in powers of δ and collecting similar terms, equations (8a), (8b) and (8c) become

$$\frac{1}{4} (\sigma_{xx}^{(0)} - \sigma_{yy}^{(0)})^2 + \sigma_{xy}^{(0)2} + \delta \left(\frac{1}{2} (\sigma_{xx}^{(0)} - \sigma_{yy}^{(0)}) (\sigma_{xx}^{(1)} - \sigma_{yy}^{(1)}) + 2\sigma_{xy}^{(0)} \sigma_{xy}^{(1)} \right) \quad (16a)$$

$$+ \delta^2 \left(\frac{1}{4} [(\sigma_{xx}^{(1)} - \sigma_{yy}^{(1)})^2 + 2(\sigma_{xx}^{(0)} - \sigma_{yy}^{(0)}) (\sigma_{xx}^{(2)} - \sigma_{yy}^{(2)})] + \sigma_{xy}^{(1)2} + 2\sigma_{xy}^{(0)} \sigma_{xy}^{(2)} \right) + O(\delta^3) = 1,$$

$$\frac{\partial \sigma_{xy}^{(0)}}{\partial y} + \delta \left(\frac{\partial \sigma_{xx}^{(0)}}{\partial z} + \frac{1}{h(z)} \frac{\partial \sigma_{xx}^{(1)}}{\partial n} + \frac{\partial \sigma_{xy}^{(1)}}{\partial y} \right) + \delta^2 \left(\frac{\partial \sigma_{xx}^{(1)}}{\partial z} + \frac{1}{h(z)} \frac{\partial \sigma_{xx}^{(2)}}{\partial n} + \frac{\partial \sigma_{xy}^{(2)}}{\partial y} \right) + O(\delta^3) = 0, \quad (16b)$$

$$\frac{\partial \sigma_{yy}^{(0)}}{\partial y} + \delta \left(\frac{\partial \sigma_{yy}^{(1)}}{\partial y} + \frac{\partial \sigma_{xy}^{(0)}}{\partial z} + \frac{1}{h(z)} \frac{\partial \sigma_{xy}^{(1)}}{\partial n} \right) + \delta^2 \left(\frac{\partial \sigma_{yy}^{(2)}}{\partial y} + \frac{\partial \sigma_{xy}^{(1)}}{\partial z} + \frac{1}{h(z)} \frac{\partial \sigma_{xy}^{(2)}}{\partial n} \right) + O(\delta^3) = 0. \quad (16c)$$

The Coulomb friction surface boundary conditions for stress from (9) becomes

$$\begin{aligned} \sigma_{xy}^{(0)} + \delta \left(\frac{dh}{dz} (\sigma_{yy}^{(0)} - \sigma_{xx}^{(0)}) + \sigma_{xy}^{(1)} \right) + \delta^2 \left(\frac{dh}{dz} (\sigma_{yy}^{(1)} - \sigma_{xx}^{(1)}) + \sigma_{xy}^{(2)} - \left(\frac{dh}{dz} \right)^2 \sigma_{xy}^{(0)} \right) + O(\delta^3) \\ = \mp \delta \left(\beta \sigma_{yy}^{(0)} \right) \mp \delta^2 \left(\beta \sigma_{yy}^{(1)} - 2\beta \frac{dh}{dz} \sigma_{xy}^{(0)} \right) + O(\delta^3). \end{aligned} \quad (17)$$

Forward/backward tension per unit width at the roll-gap entrance/exit can be expanded as

$$F_{\text{in/out}} = \int_{-1/h_{\text{in/out}}}^{1/h_{\text{in/out}}} \sigma_{xx}^{(0)}(0, y) dy + \delta \int_{-1/h_{\text{in/out}}}^{1/h_{\text{in/out}}} \sigma_{xx}^{(1)}(0, y) dy + O(\delta^2). \quad (18)$$

Shear stress is assumed to have a known distribution at the entrance, $\delta\tau_0$, and hence

$$\sigma_{xy}(z = n = 0) = 0 + \delta\tau_0 + O(\delta^2), \quad (19)$$

Finally, symmetry condition implies that σ_{xy} is zero at all orders of δ about the centre line at $y = 0$.

3.1.1 Leading-order Solution

At leading order, the friction equation (17) implies that $\sigma_{xy}^{(0)}$ is zero on the roll surface, and the momentum equation (16b) implies that it is independent of y . Hence, we conclude that $\sigma_{xy}^{(0)} = 0$ everywhere; i.e. the shear stress σ_{xy} is small and of order at most $O(\delta)$ throughout the roll gap. Hence, at leading order, the yield equation (16a) is reduced to

$$\frac{1}{4} \left(\sigma_{xx}^{(0)} - \sigma_{yy}^{(0)} \right)^2 = 1. \quad (20)$$

Substituting for the leading-order hydrostatic pressure $-2p^{(0)} = \sigma_{xx}^{(0)} + \sigma_{yy}^{(0)}$, we therefore have

$$\sigma_{xx}^{(0)} = 1 - p^{(0)} \quad \text{and} \quad \sigma_{yy}^{(0)} = -1 - p^{(0)}, \quad (21)$$

where we have asserted that σ_{yy} is more compressive than σ_{xx} . From momentum conservation equation (16c) at leading order, $\sigma_{yy}^{(0)}$ is independent of y , and so consequently are $p^{(0)}$ and $\sigma_{xx}^{(0)}$. This implies that both normal stress components are vertically homogeneous at this order. The solution for $p^{(0)}(z)$ will be dictated by satisfying the friction expression (17) at $O(\delta)$ on the surface, although this involves the as-yet-unknown $\sigma_{xy}^{(1)}$, and so we must first solve the first-order equations before $p^{(0)}$ can be fully determined. Boundary conditions for $p^{(0)}$ are determined by the prescribed front and back tension at the entrance and exit (18),

$$p^{(0)}(z = 0) = 1 - \frac{F_{\text{in}}}{2} \quad \text{and} \quad p^{(0)}(z = 1) = 1 - \frac{F_{\text{out}}}{2h(1)}. \quad (22)$$

3.1.2 First-order Solution

By taking the terms of order δ in the yield function (16a), and from the definition of hydrostatic pressure, $\sigma_{xx}^{(1)}$ and $\sigma_{yy}^{(1)}$ are given by

$$\sigma_{xx}^{(1)}(n, y, z) = \sigma_{yy}^{(1)}(n, y, z) = -p^{(1)}(n, y, z). \quad (23)$$

The momentum conservation equations (16b) and (16c) at this order then become

$$\frac{\partial \sigma_{xy}^{(1)}}{\partial y} - \frac{1}{h(z)} \frac{\partial p^{(1)}}{\partial n} = \frac{dp^{(0)}}{dz} \quad \text{and} \quad \frac{\partial p^{(1)}}{\partial y} - \frac{1}{h(z)} \frac{\partial \sigma_{xy}^{(1)}}{\partial n} = 0. \quad (24)$$

These two equations give wave equations for $p^{(1)}$ and $\sigma_{xy}^{(1)}$, forced by the leading-order pressure gradient, with solution

$$p^{(1)} = A \left(n + \frac{y}{h}, z \right) + A \left(n - \frac{y}{h}, z \right) + D(z), \quad (25a)$$

$$\sigma_{xy}^{(1)} = A \left(n + \frac{y}{h}, z \right) - A \left(n - \frac{y}{h}, z \right) + y \frac{dp^{(0)}}{dz}. \quad (25b)$$

The function $A(\xi, z)$ here is the as-yet-unknown wave solution, and we have made use of the fact that p is symmetric in y and σ_{xy} is asymmetric. $D(z)$ is a constant of integration with respect to n and y , and so is only a function of the slow variable z . Equations (25a) and (25b) are travelling waves in the fast axial variable n , and hence result in rapid stress oscillations. This finding distinguishes this study from previous asymptotic models, where all horizontal behaviour was assumed to be at the long length scale, and consequently such oscillatory patterns were not captured.

With the general form of the solution for $\sigma_{xy}^{(1)}$ now known, we may now solve for $p^{(0)}$, which remained undetermined at leading order. At $O(\delta)$, the Coulomb friction equation (17) is

$$-2\frac{dh}{dz} + \sigma_{xy}^{(1)} \mp \beta(1 + p^{(0)}) = 0. \quad (26)$$

Substituting $\sigma_{xy}^{(1)}$ from (25b) into (26) and evaluating at $y = h$ results in

$$-2\frac{dh}{dz} \mp \beta(1 + p^{(0)}) + h\frac{dp^{(0)}}{dz} = -(A(n+1, z) - A(n-1, z)), \quad (27)$$

where the left-hand side is a function of the slow variable z only and is independent of the fast variable n . We can therefore interpret (27) as a statement that A increases by a constant (with respect to n) when n increases by 2. If the constant is non-zero, A grows as a function of n , and by the end of the roll gap, $p^{(1)}$ or $\sigma_{xy}^{(1)}$ would be $O(n) = O(1/\delta)$ and the asymptotic ordering we assumed in deriving our equations would be broken [33]. Therefore, we require this constant to be zero, for $p^{(1)}$ and $\sigma_{xy}^{(1)}$ to remain bounded in terms of n , i.e.

$$A(n+1, z) - A(n-1, z) = 0. \quad (28)$$

We also note that (25) allows A to be shifted by any finite function of z , which is then absorbed into D ; for simplicity we define D by setting

$$\int_{-1}^1 A(\xi, z) d\xi = 0. \quad (29)$$

Substituting (28) into (27) gives a first-order ordinary differential equation (ODE) for $p^{(0)}(z)$ as,

$$-2\frac{dh}{dz} \mp \beta(1 + p^{(0)}) + h\frac{dp^{(0)}}{dz} = 0. \quad (30)$$

This is analogous to the ODE for $\sigma_{yy}^{(0)}$ derived previously by Minton et al. [26] for asymmetric thin sheet rolling and by Cawthorn et al. [30] for sandwich rolling. This can be solved with the boundary conditions (22) once from the entrance forwards with $-ve$ sign of the coefficient of the friction term and once from the exit backwards with $+ve$ sign. These two solutions cross at the point which determines the location of the neutral point z_N , and the whole solution gives the expected ‘‘pressure hill’’ obtained from the classical slab method. In fact, the approximation obtained here by the asymptotic analysis at leading order (by restricting the effect of shear stress to a small contribution on the surface) is identical to that obtained by the slab method.

Returning to the first-order solution presented in (25), we now consider the two unknown functions $A(\xi, z)$ and $D(z)$. Condition (28) establishes that, as a function of ξ , A is periodic with period 2. This means A needs only be found for $-1 < \xi < 1$ as z varies to be fully determined. Finding the z -dependency of the function A , as well as the unknown $D(z)$, requires further information which will be revealed in the next order of correction. However, the boundary condition at the entrance provides the initial conditions. Since F_{in} has already been satisfied at leading order, the first-order correction to it must be zero. Hence, according to equation (18) and using condition (29),

$$\int_{-h_0}^{h_0} \sigma_{xx}^{(1)}(y, 0) dy = - \int_{-1}^1 (A(y, 0) + A(-y, 0) - D(0)) dy = 0 \quad \Rightarrow \quad D(0) = 0. \quad (31)$$

which is an initial condition for $D(z)$. Moreover, from (23) and (25), at $z = 0$ where $h = 1$ and $n = 0$, we have $\sigma_{xx}^{(1)}(y, 0) = -A(y, 0) - A(-y, 0)$ and $\tau_0 = A(y, 0) - A(-y, 0) + y dp^{(0)}/dz$, and consequently,

$$A(y, 0) = \frac{1}{2} \left(\tau_0(y) - \sigma_{xx}^{(1)}(y, 0) \right) - \frac{1}{2} y \frac{dp^{(0)}}{dz} \Big|_{z=0}, \quad (32)$$

where $\tau_0(y)$ is the known distribution of shear stress at the entrance according to (19). Equation (32) gives an initial condition for A at $z = 0$ for a given distribution of normal and shear stress at the entrance ($\sigma_{xx}^{(1)}(y, 0)$ and $\tau_0(y)$ respectively), and will be discussed later in Section 4.1.

3.1.3 Second-order Solution

The solution is continued to this order of correction with the goal of finding the unknown parameters $A(\xi, z)$ and $D(z)$ from the previous order. Using the stress equations in Section 3.1 at $O(\delta^2)$, and after significant algebra detailed in Appendix A, the following expression is derived:

$$2h \frac{\partial A(n+1, z)}{\partial z} + \frac{\partial}{\partial n} (A(n+1, z)^2) + \left(h \frac{dp^{(0)}}{dz} \mp 2\beta \right) A(n+1, z) - h \frac{dD}{dz} \mp \beta D(z) = 0. \quad (33)$$

By integrating (33) between $n = -2$ and $n = 0$ and imposing (29), we arrive at

$$-h \frac{dD}{dz} \mp \beta D(z) = 0. \quad (34)$$

Since $D(0) = 0$ from (31), we conclude that $D(z) \equiv 0$. With this, equation (33) then gives an evolution equation for how A varies as z is increased,

$$2h \frac{\partial A(\xi, z)}{\partial z} + \frac{\partial}{\partial \xi} (A(\xi, z)^2) + \left(h \frac{dp^{(0)}}{dz} \mp 2\beta \right) A(\xi, z) = 0. \quad (35)$$

This partial differential equation cannot be solved exactly, so a numerical approach is needed. We can simplify the numerics required by introducing variables $\alpha_1(z)$, $T(z)$ and $\omega(\xi, T)$, as shown in Appendix B;

$$T = \int^z \frac{\alpha_1}{h(\bar{z})^2} d\bar{z}, \quad \omega(\xi, T(z)) = \frac{A(\xi, z)}{(\alpha_1/h)} \quad \text{and} \quad \alpha_1 = \exp \left\{ \int_0^z \left[\mp \frac{\beta}{2h(\bar{z})} (p^{(0)}(\bar{z}) - 1) \right] d\bar{z} \right\}, \quad (36a)$$

$$\Rightarrow \quad \frac{\partial \omega}{\partial T} + \frac{1}{2} \frac{\partial}{\partial \xi} (\omega^2) = 0. \quad (36b)$$

Equation (36b) is a standard Burger's equation which is especially advantageous as it enables the effective handling of the evolution of discontinuities in the form of shocks or expansion fans.

Once (36b) has been solved with suitable initial conditions for ω and hence A , the correction to the pressure, $p^{(1)}$, and all the components of the Cauchy stress, $\sigma_{xx}^{(1)}$, $\sigma_{yy}^{(1)}$ and $\sigma_{xy}^{(1)}$, can be calculated by evaluating (25a), (23) and (25b) respectively. It should be noted that, since the boundary condition changes on the surface at the neutral point, equation (36b) should be solved separately for the entrance and exit regions, with the two regions connected at the neutral point. The behaviour in the vicinity of this neutral point is discussed further in the next section.

3.1.4 Behaviour near the neutral point

The shear stress $\sigma_{xy}^{(1)}$, given in equation (25b), is formed of two components: the first component involving A will be seen to cause a wave pattern, while the second one, $y dp^{(0)}/dz$, varies linearly through the thickness with a gradient proportional to the gradient of $p^{(0)}$. The term $y dp^{(0)}/dz$ changes suddenly at the neutral point, which could hypothetically cause a discontinuity in shear stress across a straight line running through the thickness of the sheet perpendicular to its longitudinal axis, as illustrated in the right panel of Figure 3. This discontinuity is predicted by many mathematical models for cold rolling that use Coulomb friction [26, 28, 29, 38]. Physically, the sudden change in sign of the shear stress at the surface is an expected consequence of Coulomb friction. However, any through-thickness discontinuity must be artificial, since otherwise vertical forces would not balance on the thin vertical slice of material at the neutral point due to change in the direction of the vertical component of shear stress. Instead, we require σ_{xy} to be continuous in z . Introducing the notation $(-)$ and $(+)$ to denote variables to the left and right of the neutral point respectively, near the neutral point $z = z_N$ we require $\sigma_{xy}^{(1-)} = \sigma_{xy}^{(1+)}$. Therefore from (25b) we obtain,

$$\begin{aligned} A^{(-)} \left(n + \frac{y}{h}, z \right) - A^{(-)} \left(n - \frac{y}{h}, z \right) + \frac{h_N}{2} \left[\left(n + \frac{y}{h}, z \right) - \left(n - \frac{y}{h}, z \right) \right] \frac{dp^{(0-)}}{dz} \Big|_{z=z_N} \\ = A^{(+)} \left(n + \frac{y}{h}, z \right) - A^{(+)} \left(n - \frac{y}{h}, z \right) + \frac{h_N}{2} \left[\left(n + \frac{y}{h}, z \right) - \left(n - \frac{y}{h}, z \right) \right] \frac{dp^{(0+)}}{dz} \Big|_{z=z_N}. \end{aligned} \quad (37)$$

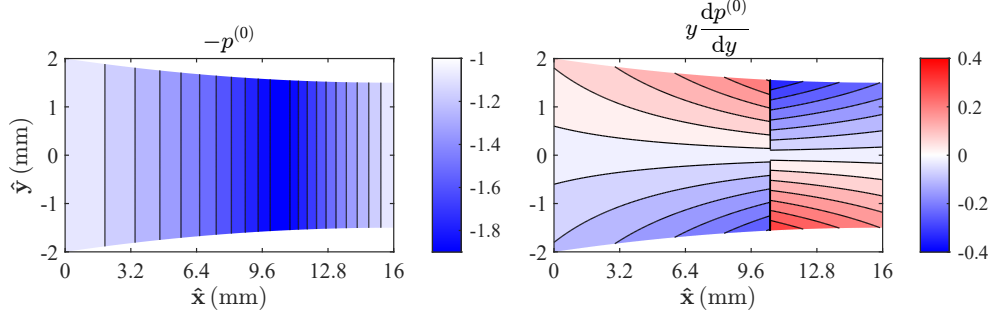


Figure 3: Leading-order pressure (left) and the term $y dp^{(0)}/dy$ (right), which contributes to shear. Results are shown in dimensionless form, i.e. scaled with $\hat{\kappa}$, the yield stress in shear. Parameters used are $(\hat{h}_0, \delta, r, \mu) = (2 \text{ mm}, 0.125, 25\%, 0.1)$.

Solving (37) and applying (30) yields

$$A^{(+)}(\xi, z_N) = A^{(-)}(\xi, z_N) + \frac{h_N}{2} \left(\left. \frac{dp^{(0-)}}{dz} \right|_{z=z_N} - \left. \frac{dp^{(0+)}}{dz} \right|_{z=z_N} \right) = A^{(-)}(\xi, z_N) + \beta \xi \left(1 + p^{(0)}(z_N) \right). \quad (38)$$

In this derivation, it is assumed that there is no $O(\delta)$ correction to the location of the neutral point, and that the change from $A^{(-)}$ to $A^{(+)}$ happens abruptly. These assumptions are verified via a more thorough calculation about the neutral point in Appendix C. Since both $A^{(-)}$ and $A^{(+)}$ are periodic in ξ with period 2, equations (38) completely define $A^{(+)}(\xi, z_N)$ in terms of $A^{(-)}$, from which equation (35) or (36b) can be used to evolve $A^{(+)}$ for $z_N < z < 1$, giving the full solution in the entire roll gap. Note that $A^{(-)}$ is known completely from the initial conditions (32) at $z = 0$ and then solving equation (35) or (36b) for $0 < z < z_N$.

3.2 Solving for the Velocities

Having solved for the stresses in Section 3.1, we now begin the calculation of the velocity field. The approach here is the same as was used for the stresses above. By asymptotically expanding equations (8d), (8e) and (8f) in successive powers of δ and collecting like terms we obtain,

$$\frac{\partial v^{(0)}}{\partial y} + \delta \left(\frac{\partial u^{(0)}}{\partial z} + \frac{1}{h(z)} \frac{\partial u^{(1)}}{\partial n} + \frac{\partial v^{(1)}}{\partial y} \right) + \delta^2 \left(\frac{\partial u^{(1)}}{\partial z} + \frac{1}{h(z)} \frac{\partial u^{(2)}}{\partial n} + \frac{\partial v^{(2)}}{\partial y} \right) + O(\delta^3) = 0, \quad (39a)$$

$$\delta \left(\frac{\partial u^{(0)}}{\partial z} + \frac{1}{h(z)} \frac{\partial u^{(1)}}{\partial n} \right) + \delta^2 \left(\frac{\partial u^{(1)}}{\partial z} + \frac{1}{h(z)} \frac{\partial u^{(2)}}{\partial n} \right) + O(\delta^3) = \frac{1}{2} \lambda^{(0)} (\sigma_{xx}^{(0)} - \sigma_{yy}^{(0)}) + \frac{\delta}{2} \left(\lambda^{(0)} (\sigma_{xx}^{(1)} - \sigma_{yy}^{(1)}) + \lambda^{(1)} (\sigma_{xx}^{(0)} - \sigma_{yy}^{(0)}) \right) + O(\delta^2), \quad (39b)$$

$$\frac{\partial u^{(0)}}{\partial y} + \delta \left(\frac{\partial u^{(1)}}{\partial y} + \frac{\partial v^{(0)}}{\partial z} + \frac{1}{h(z)} \frac{\partial v^{(1)}}{\partial n} \right) + \delta^2 \left(\frac{\partial u^{(2)}}{\partial y} + \frac{\partial v^{(1)}}{\partial z} + \frac{1}{h(z)} \frac{\partial v^{(2)}}{\partial n} \right) + O(\delta^3) = 2\sigma_{xy}^{(0)} \lambda^{(0)} + 2\delta \left(\lambda^{(0)} \sigma_{xy}^{(1)} + \lambda^{(1)} \sigma_{xy}^{(0)} \right) + 2\delta^2 \left(\lambda^{(0)} \sigma_{xy}^{(2)} + \lambda^{(1)} \sigma_{xy}^{(1)} + \lambda^{(2)} \sigma_{xy}^{(0)} \right) + O(\delta^3). \quad (39c)$$

The surface boundary condition for velocity from (12) is,

$$v^{(0)} + \delta v^{(1)} + \delta^2 v^{(2)} + O(\delta^3) = \delta \frac{dh}{dz} \left(u^{(0)} + \delta u^{(1)} \right) + O(\delta^3). \quad (40)$$

For the velocity initial condition, the sheet is assumed to enter as a rigid stock with a strictly horizontal velocity, meaning that $v^{(1)} \equiv u^{(1)} \equiv 0$ at $z = 0$. Thus, equation (11) is expanded as,

$$u(z = n = 0) = 1 + \delta(0) + \delta^2(0) + O(\delta^3) \quad \text{and} \quad v(z = n = 0) = 0 + \delta(0) + \delta^2(0) + O(\delta^3) \quad (41)$$

Finally, symmetry condition (13) implies v is zero at all orders of δ about the centre line at $y = 0$.

3.2.1 Leading-order

Evaluating (39c) at leading order yields

$$\frac{\partial u^{(0)}}{\partial y} = 0, \quad (42)$$

indicating $u^{(0)}$ is uniform across the sheet thickness, as was found for the stress components at this order. Evaluating the averaged mass equation (14) at leading order then yields

$$u^{(0)}(z) = \frac{1}{h(z)}. \quad (43)$$

The vertical velocity at leading order, $v^{(0)}$, is identically zero. This can be determined by evaluating the continuity equation (39a) at leading order to show that $v^{(0)}$ is independent of y , and using the no-penetration boundary condition (40), which imposes zero vertical velocity $v^{(0)}$ on the surface. Based on the tension flow rule equation (39b), the leading-order plastic multiplier $\lambda^{(0)}$ is also found to be zero.

3.2.2 First-order

By only taking terms of order δ , the continuity equation (39a) and the shear flow-rule equation (39c) become, respectively,

$$\frac{\partial v^{(1)}}{\partial y} + \frac{1}{h} \frac{\partial u^{(1)}}{\partial n} = -\frac{\partial u^{(0)}}{\partial z} \quad \text{and} \quad \frac{\partial u^{(1)}}{\partial y} + \frac{1}{h} \frac{\partial v^{(1)}}{\partial n} = 0. \quad (44)$$

Therefore, similar to the stresses at this order, $u^{(1)}$ and $v^{(1)}$ satisfy a wave equation with the general solution

$$u^{(1)} = B\left(n + \frac{y}{h}, z\right) + B\left(n - \frac{y}{h}, z\right), \quad (45a)$$

$$v^{(1)} = -\left[B\left(n + \frac{y}{h}, z\right) - B\left(n - \frac{y}{h}, z\right)\right] + \frac{y}{h^2} \frac{dh}{dz}, \quad (45b)$$

where $B(\xi, z)$ is an unknown function. The solution above has accounted for the symmetry of u and asymmetry of v with respect to y . By substituting the solution for $v^{(1)}$ into the tension flow-rule equation (39b), $\lambda^{(1)}$ is found to be

$$\lambda^{(1)} = -\frac{\partial v^{(1)}}{\partial y} = \frac{1}{h} \left[B'\left(n + \frac{y}{h}, z\right) + B'\left(n - \frac{y}{h}, z\right) \right] - \frac{1}{h^2} \frac{dh}{dz}, \quad (46)$$

with prime denoting $\partial/\partial\xi$. As a result of the no-penetration boundary condition on the surface (40),

$$v^{(1)}(y = h) = \frac{dh}{dz} u^{(0)} \quad \Rightarrow \quad B(n + 1, z) = B(n - 1, z), \quad (47)$$

which implies that $B(\xi, z)$ is periodic with periodicity 2, similarly to $A(\xi, z)$ for the stresses. This means B needs only be defined for $-1 < \xi < 1$ for each value of z . Initial condition for $B(\xi, z)$ at the entrance, is given by setting $n = z = 0$ in (45) and subtracting equation (45b) from (45a). By imposing zero first-order horizontal and vertical velocities at the entrance from (41) we then have:

$$B(y, 0) = \frac{y}{2} \frac{dh}{dz} \Big|_{z=0}. \quad (48)$$

Additional information is required to determine the evolution of this initial condition with respect to z (i.e. the z dependency of the function B), which is discussed below.

3.2.3 Second-order

The continuity equation (39a) and the shear flow-rule equation (39c), at order δ^2 are, respectively,

$$\frac{\partial v^{(2)}}{\partial y} + \frac{1}{h} \frac{\partial u^{(2)}}{\partial n} = -\frac{\partial u^{(1)}}{\partial z}, \quad (49a)$$

$$\frac{\partial u^{(2)}}{\partial y} + \frac{1}{h} \frac{\partial v^{(2)}}{\partial n} = -\frac{\partial v^{(1)}}{\partial z} + 2\lambda^{(1)}\sigma_{xy}^{(1)}. \quad (49b)$$

By substituting the solutions obtained thus far into equation (49), we arrive at a wave equation for $u^{(2)}$ and $v^{(2)}$ driven by terms involving $A(\xi, z)$ and $B(\xi, z)$. Details of this and its solution are given in Appendix D. Avoiding a growing term, as for the stresses, results in an evolution equation in z for B given by

$$\frac{\partial B(n+1, z)}{\partial z} - \frac{1}{h^2} \frac{dh}{dz} A(n+1, z) - \left(\frac{1}{2} \frac{dp^{(0)}}{dz} - \frac{1}{h} \frac{dh}{dz} \right) B(n+1, z) + \frac{1}{h} B'(n+1, z) A(n+1, z) = 0. \quad (50)$$

This equation can be simplified by defining $\alpha_2(z) = \exp\{\frac{1}{2}p^{(0)}\}$, to give,

$$\frac{\partial}{\partial z} \left(\frac{B(\xi, z)}{(\alpha_2/h)} \right) + \frac{A(\xi, z)}{h} \frac{\partial}{\partial \xi} \left(\frac{B(\xi, z)}{(\alpha_2/h)} \right) = \frac{1}{h\alpha_2} \frac{dh}{dz} A(\xi, z). \quad (51)$$

This is an advection equation with a velocity of $A(\xi, z)/h$. It is, however, more convenient to solve the equation if the excitation term on the right hand side can be included inside the derivatives. Moreover, when compared to Burger's equation for the stresses (36b), the above equation can be rewritten to have the same advection speed $\omega(\xi, z)$. The derivation of this rearranged equation is also given in Appendix E, finally yielding the genuine advection equation

$$\frac{\partial}{\partial T} \left(\frac{B}{(\alpha_2/h)} - Q\omega \right) + \omega \frac{\partial}{\partial \xi} \left(\frac{B}{(\alpha_2/h)} - Q\omega \right) = 0, \quad \text{where } Q(z) = \int_0^z \frac{\alpha_1}{\alpha_2 h^2} \frac{dh}{d\tilde{z}} d\tilde{z}. \quad (52)$$

Equation (52) or (51) can be solved with a suitable initial condition, and the solution B can be subsequently used to calculate $u^{(1)}$, $v^{(1)}$ and $\lambda^{(1)}$ by evaluating (45a), (45b) and (46) respectively.

4 Computing the asymptotic solutions

Above we have derived governing equations for the various components of stress and strain that can be integrated through the roll gap, either analytically or semi-analytically, starting from initial conditions at the roll-gap entrance and matching some conditions at the roll-gap exit. In this section, we summarise the solutions gained thus far and detail a simple numerical procedure for performing these calculations. We begin by considering the stresses, since they may be solved independently of the velocities.

4.1 Stresses

The stress profiles in terms of horizontal distance x , and vertical distance y are written in terms of horizontal scales $n = \int_0^x 1/h dx$ and $z = \delta x$ as

$$p = p^{(0)}(z) + \delta \left[A\left(n + \frac{y}{h}, z\right) + A\left(n - \frac{y}{h}, z\right) \right] + O(\delta^2) \quad (53a)$$

$$\sigma_{xy} = 0 + \delta \left[A\left(n + \frac{y}{h}, z\right) - A\left(n - \frac{y}{h}, z\right) + y \frac{dp^{(0)}}{dz} \right] + O(\delta^2), \quad (53b)$$

$$\sigma_{xx} = 1 - p, \quad (53c)$$

$$\sigma_{yy} = -1 - p. \quad (53d)$$

The leading-order pressure $p^{(0)}(z)$ is given by,

$$\frac{dp^{(0)}}{dz} - \beta(1 + p^{(0)}) - 2\frac{dh}{dz} = 0, \quad \text{for } z < z_N \quad \text{with } p^{(0)}(z=0) = 1, \quad (54a)$$

$$\frac{dp^{(0)}}{dz} + \beta(1 + p^{(0)}) - 2\frac{dh}{dz} = 0, \quad \text{for } z > z_N \quad \text{with } p^{(0)}(z=1) = 1, \quad (54b)$$

with z_N chosen such that $p^{(0)}$ is continuous at z_N . The solution for $p^{(0)}$ is chosen to satisfy the forward and backward tension conditions, which are taken to be zero for the results presented below. Therefore, $p^{(0)}$ is solved by integrating equation (54a) forward from the entrance, and integrating equation (54b) backwards from the exit, using the MATLAB ODE solver `ode45` [39]. This is the same solution as the slab method and the two curves thus produced are referred to as the friction hill. The location of the intersection of the curves defines the location of the neutral point at leading order.

The first-order wave-like oscillatory function $A(\xi, z)$, in the set of equations (53), obeys Burger's equation once suitably rescaled,

$$A(\xi, z) = \frac{\alpha_1}{h} \omega(\xi, T(z)), \quad \frac{\partial \omega}{\partial T} + \frac{1}{2} \frac{\partial}{\partial \xi} (\omega^2) = 0 \quad \text{for } -1 < \xi < 1, \quad (55a)$$

$$T = \int^z \frac{\alpha_1}{h(\bar{z})^2} d\bar{z}, \quad \alpha_1 = \exp \left\{ \int_0^z \left(\mp \frac{\beta}{2h(\bar{z})} (p^{(0)}(\bar{z}) - 1) \right) d\bar{z} \right\}, \quad (55b)$$

with A and therefore ω are periodic in ξ such that

$$A(\xi + 1, z) = A(\xi - 1, z). \quad (56)$$

Due to periodicity, it is sufficient to solve Burger's equation for $-1 < \xi < 1$. Burger's equation (55) is solved first from the entrance at $z = 0$ to the neutral point at $z = z_N$ to give $A^{(-)}$, and is then solved again from $z = z_N$ onwards with the new initial condition at the neutral point to give $A^{(+)}$:

$$A(\xi, z) = \begin{cases} A^{(-)}(\xi, z) & \text{for } z < z_N & \text{with } A^{(-)}(\xi, 0) = \frac{1}{2} \left(\tau_0(\xi) - \sigma_{xx}^{(1)}(\xi, 0) \right) - \frac{1}{2} \xi \frac{dp^{(0)}}{dz} \Big|_{z=0} \\ A^{(+)}(\xi, z) & \text{for } z > z_N & \text{with } A^{(+)}(\xi, z_N) = A^{(-)}(\xi, z_N) + \beta \xi (p^{(0)}(z_N) + 1). \end{cases} \quad (57)$$

For the initial condition at $n = z = 0$ in (57), the simplest assumption is that $\sigma_{xx}^{(1)}$ is zero and $\tau_0(y)$ is linear in y at the entrance. This implies a situation where all material points are affected the same by the inlet tension, and the shear stress linearly increases from zero at the symmetry line to its maximum value at the surface. While this maximum shear stress can be chosen to give good agreement with FE results, as will be seen below, an improved estimation is obtained by allowing $\sigma_{xx}^{(1)}$ to vary quadratically (but with average value zero to maintain the same inlet tension according to (18)). Both scenarios are compared with FE results in Section 5. Once $A^{(-)}$ is completely solved from (55) with the initial conditions at $n = z = 0$, the solution at z_N is used to modify the initial condition at the neutral point. This new initial condition is then used to solve $A^{(+)}$ from the neutral point to the exit. $A^{(-)}$ and $A^{(+)}$ together give the full solution in the entire roll gap.

Burger's equation (55) is solved with the finite volume method in MATLAB, and a limiter is applied to ensure that the numerical solution does not develop new extrema. While the periodicity of A in ξ means that A will have discontinuities (e.g. at $\xi = \pm 1$), these discontinuities form an expansion fan in the Burger's equation solution, and so are not problematic. Using the unoptimised MATLAB code provided in the supplementary material, solving for all stresses takes of the order of a couple of seconds on a standard laptop.

4.2 Velocity

The velocity profiles are given by,

$$u = \frac{1}{h} + \delta \left[B\left(n + \frac{y}{h}, z\right) + B\left(n - \frac{y}{h}, z\right) \right] + O(\delta^2), \quad (58a)$$

$$v = 0 - \delta \left[B\left(n + \frac{y}{h}, z\right) - B\left(n - \frac{y}{h}, z\right) - y \frac{dh/dz}{h^2} \right] + O(\delta^2), \quad (58b)$$

where the leading-order slab-like behaviour is controlled directly by the roll-gap thickness imposed by the rolls, and the wave-like oscillatory correction obeys,

$$\frac{\partial}{\partial T} \left(\frac{B}{(\alpha_2/h)} - Q\omega \right) + \omega \frac{\partial}{\partial \xi} \left(\frac{B}{(\alpha_2/h)} - Q\omega \right) = 0 \quad \text{for } -1 < \xi < 1 \quad \text{with } B(\xi, 0) = \frac{\xi}{2} \frac{dh}{dz} \Big|_{z=0}, \quad (59a)$$

$$Q(z) = \int_0^z \frac{\alpha_1}{\alpha_2 h^2} \frac{dh}{d\bar{z}} d\bar{z}, \quad \alpha_2(z) = \exp \left\{ \frac{1}{2} p^{(0)} \right\}, \quad (59b)$$

and with periodicity $B(\xi + 1, z) = B(\xi - 1, z)$, as for $A(\xi, z)$.

Similarly to $A(\xi, z)$, the advection equation (59) may be fully solved for $B(\xi, z)$ using suitable initial conditions at $z = 0$ for $-1 < \xi < 1$, with discontinuities at the beginning and end of each interval forced by the periodic nature of $B(\xi, z)$, similar to $A(\xi, z)$, which again results in an expansion fan.

A subtlety of the solution here, however, unlike the Burger’s equation solution for $A(\xi, z)$, is that a discontinuous initial condition coupled with the advection equation for $B(\xi, z)$ does not completely determine the solution within the expansion fan. This distinction arises because, in Burger’s equation, the function within an expansion fan is inversely proportional to the slope of characteristic lines, a relationship which does not apply to the advection equation. Consequently, additional information is needed to specify the initial condition for the expansion fan for $B(\xi, z)$. Physically, this might come from solving an inner elastic problem at the contact point at the entrance, a topic not addressed in this study. Consequently, here we assume that, as for Burger’s equation, the expansion fan is initially linear, and instead of specifying $B(\xi, z)$ at $z = 0$ and integrating forwards, we specify $B(\xi, z)$ for a small nonzero value of z close to the entrance and solve for the evolution forward to the exit and backward to the entrance using the advection equation (59). This allows us to use a continuous initial condition for our solver, chosen such that the solution at the entrance is the desired one.

The numerical solution to (59) is non-trivial, with the advected velocity depending on both ξ and z and being positive and negative. Here, an upwinding explicit finite difference method is employed. The computation time varies with the step size in order to maintain a CFL constraint, but the results plotted here are obtained in a few seconds using unoptimised MATLAB code on a standard laptop.

5 Results and comparison with FE simulation

Since it is extremely difficult to experimentally observe the stress pattern through thickness during the rolling process, the predictions of the asymptotic model are here compared with carefully conducted FE simulations using the ABAQUS package; full details are given by Flanagan et al. [8]. In summary, simulations are made in ABAQUS/Standard with an implicit solver. Only one roll and half the sheet are simulated following the assumption of symmetry about the sheet’s horizontal centre plane. To comply with the plane-strain assumption, the sheet metal is modelled as a two-dimensional deformable part and the rolls as a two-dimensional analytical rigid geometry. The contact between the roll and sheet is discretised using the surface-to-surface method. Since a mesh sensitivity study confirmed that under-resolution through-thickness strongly affects the results [8], here, 30 CPE4R elements were used through the half-thickness of the sheet; this showed the best trade-off between accuracy and computation time [8]. The simulation consists of two steps: the bite step, where the roll is slowly translated vertically to indent the sheet; and the rolling step, where the sheet is horizontally displaced due to rotation of the roll. The model is then run for a sufficiently long time to attain a steady state, as measured by obtaining steady through-thickness stress and strain distributions, rather than simply by observing roll force and torque [8]. For static ABAQUS/Standard simulations, although stresses are generated directly, velocity must be calculated from the displacement change between time frames. The computation time for these simulations depends on the aspect ratio, and an example of $\delta = 0.125$ requires a computation time of 15.89 hours.

For the simulations, the sheet material is chosen to be a mild steel (grade DC04), a common material used in cold metal forming [40]. While the mathematical model uses $\hat{\kappa} = 288.67$ MPa (corresponding to $\hat{Y} = 500$ MPa), the FE simulations were performed with two different material models. Initially, simulations were performed with the yield stress of the material fixed at $\hat{\kappa} = 288.67$ MPa, so that the simulation is close to the perfectly-plastic material assumed in the current asymptotic model; this assumption is then relaxed and a more typical hardening profile is used subsequently, where the material deforms plastically from an initial yield stress of $\hat{\kappa} = 275.51$ MPa and reaches 324.29 MPa at a true plastic strain of 0.4 as a result of strain hardening. The results presented below are for the non-hardening material model unless otherwise stated. A realistic Young’s modulus of $E = 206.3$ GPa and a Poisson ratio $\nu = 0.3$ are used for all FE simulations.

For the FE simulations, the rolls rotate with a surface speed of 1.28 ms^{-1} , the sheet has an initial full thickness $2\hat{h}_0 = 4$ mm, and the size and position of the rolls is varied to give the required roll-gap aspect ratio and a reduction of $r = 0.25$. The friction coefficient between the workpiece and the rolls is chosen to be 0.1, except for short roll gaps with $\delta = 0.3$ and 0.5, for which $\mu = \delta/2$ is chosen to guarantee the initial bite. These choices of material, friction coefficient, initial thickness, reduction, and roll speed are purely illustrative, and solutions may be found for any values of these parameters.

5.1 Prediction of through-thickness variation

In Figure 4, we compare the axial stress σ_{xx} , hydrostatic pressure $-p$, and shear stress σ_{xy} predicted by the ABAQUS simulation and the current mathematical model for $\delta = 0.125$ with zero backwards/forwards

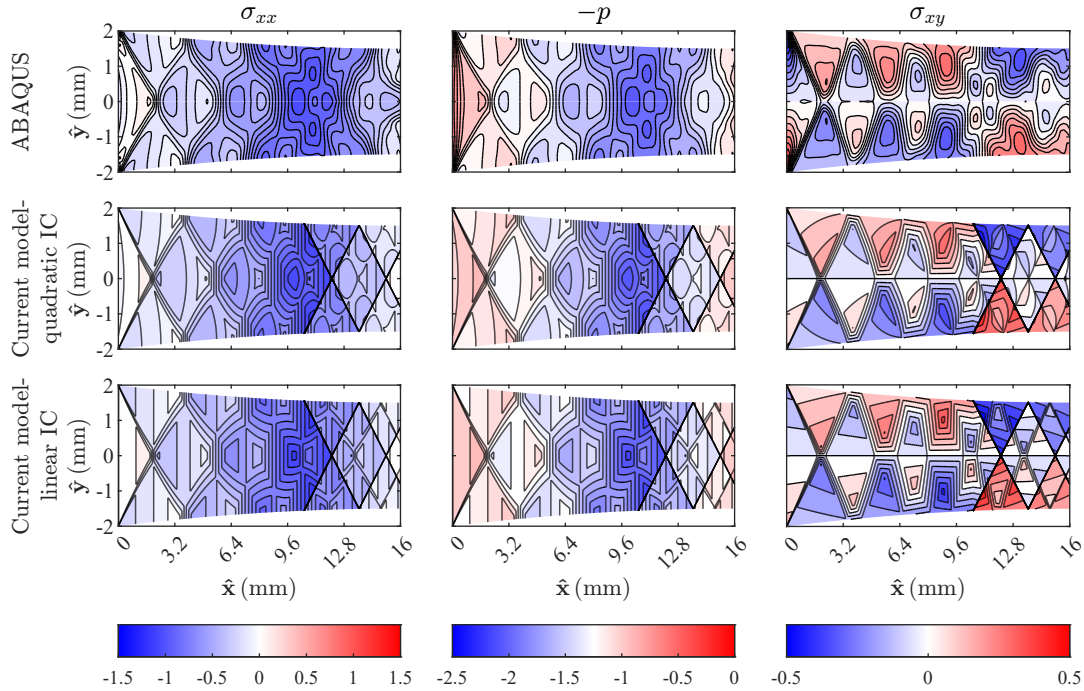


Figure 4: Comparison of results for $\delta = 0.125$ from FE simulations [8] (top row) with the current model (equation 53), with two different initial conditions: quadratic initial condition (middle row) and linear initial condition (bottom row). Left: contour plots of horizontal stress. Middle: contour plots of pressure. Right: contour plots of shear stress. Results are shown in dimensionless form, i.e. scaled with $\hat{\kappa}$, the yield stress in shear. Parameters used are $(\hat{h}_0, r, \mu, \hat{\kappa}) = (2 \text{ mm}, 25\%, 0.1, 288.67 \text{ MPa})$.

tensions. The top row shows FE simulation and the two bottom rows show results from the mathematical model with two different inlet boundary conditions. According to the ABAQUS simulation in Figure 4, even with zero back tension, the distribution of σ_{xx} is non-zero at the entrance, which can be attributed to the elastic deformation at the entrance. If known, this can be included in the mathematical model by considering the quadratic function as an initial condition as explained in 4.1, and the result of this is shown in the middle row in Figure 4. In this figure, the unknown term in (57) is taken to be $\tau_0(y) - \sigma_{xx}^{(1)}(y, 0) = -2(0.15y^2 + 0.5y - 0.05)$, where the coefficients are chosen by comparing the results with simulation and imposing a zero average (18). However, reasonable results can still be obtained by disregarding the initial distribution of σ_{xx} and imposing a linear distribution for shear stress τ_0 as the initial condition (see the bottom row in Figure 4; for this case, $\tau_0 = -1.2y$ was chosen, which gives a good comparison for all rolling parameters considered here). Comparing the two bottom rows in Figure 4 also demonstrates that, with the cost of an extra degree of freedom, the quadratic initial condition results in a rounded pattern which is more similar to the FE simulation. The mathematical model’s prediction of stresses at the roll-gap exit differs from those of the FE simulation due to the workpiece unloading and becoming purely elastic, although this appears to be localised to the roll-gap exit and does not appear to affect the agreement of the solution elsewhere within the roll gap.

The oscillatory pattern in the pressure distribution shown in Figure 4 is very similar to σ_{xx} , and with a similar effect of the initial conditions at the roll-gap entrance, as is expected from equations (53c). The pressure solution is the summation of the leading-order solution describing the “pressure hill” and the $O(\delta)$ correction term causing an oscillatory pattern. As a result of the pressure hill, the pressure is seen to approximately increase in magnitude up to the neutral point ($\hat{x} \approx 10.7$) and decrease after that up to the exit point. Nevertheless, this trend is not monotonic within either of the two zones due to the correction term; each momentary increase in pressure is followed by a subsequent decrease, resulting in the formation of multiple local peaks. This means that unlike the slab method prediction the maximum pressure does not necessarily occur exactly at the neutral point.

The shear stress distribution in the last column in Figure 4 also reveals a unique distribution, which is replicated by the mathematical model. The different initial conditions in the last two rows in the σ_{xy} panel in Figure 4 do not significantly affect the shear distribution pattern. This implies that a linear variation of shear stress is sufficient to model initial condition in (57) for the remainder of this paper.

Unlike many other mathematical models, where the application of Coulomb friction is associated with a vertical discontinuity at the neutral point (as illustrated in Figure 3), the current model correctly predicts the trend of the changing sign in shear along the diagonal lines. This is shown more clearly for shorter roll gaps, plotted as the top rows in Figure 5, where the shear stress fields from FE (left column) and the mathematical model (right column) are plotted for varying $\delta = \hat{h}_0/\hat{l}$.

The discontinuity in shear stress at the surface, observed in the mathematical model in Figures 4 and 5, is an unavoidable consequence of our assumption of Coulomb friction without sticking. The shear stress discontinuity at the surface for the mathematical model causes a shock to form in the Burger's equation solution, producing the sharp line starting from the neutral point. The FE simulation, on the other hand, predicts a sticking region, giving a smoother transition between positive and negative shear at the neutral point than is observed in the mathematical model. Still, the predicted neutral point is correctly positioned compared with the FE simulations for all aspect ratios.

Another interesting feature seen in Figures 4 and 5 is the initial diagonal discontinuity in stresses emanating from the first contact point between the workpiece surface and the rolls (e.g. the top left and bottom left points in each plot); this initial discontinuity subsequently spreads out and weakens. This is the result of the evolution of the discontinuity in the initial condition (as explained in 4.1) as an expansion fan. This field is quite common in plane-strain problems at die corners or at the location of sudden changes in cross-section solved by the slip-line method [41], and is also well predicted by the current method. Significant numerical resolution at the contact points is needed for FE simulations to accurately reproduce the same behaviour.

The trend observed in Figure 5 indicates that the oscillatory pattern is not restricted to a particular aspect ratio, as similar trends are noted for all values of δ between the FE and the model. The number of lobes present increase with roll-gap length and are approximately proportional to the aspect ratio of the roll gap $1/\delta$. This can potentially be explained by the underlying mechanism of deformation. The deformation mechanism in the roll gap is effectively that of uniaxial extension, with the sheet getting longer and thinner, although forced by the rolls rather than extensive normal forces at the entrance and exit. This means the slip lines, along which information about the deformation is carried, align with the local direction of maximum shear at 45 degrees to the centre line. As information only reaches a material element along slip lines, information about initial contact with the rolls, friction, the neutral point, etc, all travel at 45 degrees to the centre line. This sets up an oscillatory pattern that repeats, because of the 45 degree angle, on average every sheet thickness, meaning the number of oscillations depends on the number of sheet thicknesses that fit into the length of the roll gap. This becomes more comprehensible when viewed alongside the velocity distribution in Figure 6.

Figure 6 shows the vertical and horizontal velocity distribution for $\delta = 0.125$ both from FE simulation and the mathematical model. The frequency at which the pattern in vertical and horizontal velocity recurs is almost the same as that observed in stresses (Figure 5). In the vertical velocity contour plots in Figure 6, as expected, the material points are pushed towards the centre line due to the presence of the rolls, although interestingly this is limited to certain regions, between which there is almost no vertical velocity. Each zone exhibits distinct horizontal and vertical velocities that are suggestive of a block gliding over its neighbouring block at a roughly constant speed; this provides another alternative interpretation of the contrasting shear signs observed in Figure 5.

The horizontal velocity distribution in Figure 6 is also notable. The solution to $u^{(0)}$, and indeed the classic slab method, both predict a smoothly increasing horizontal velocity from the entrance to the exit due to the continuity requirement. However, the inclusion of the correction term results in an increasing horizontal velocity characterised by a series of incremental steps. This can be seen in more detail in figure 7, where the horizontal velocity along the surface and along the centreline are compared from three different methods: the slab method, the current model, and FE simulations. The sheet is introduced into the roll gap horizontally at a velocity lower than that of the rolls, and initially, while the surface accelerates following contact with the roll, the centre maintains its initial velocity. This trend then reverses and the centre line advances more rapidly than the surface. This leapfrogging of surface and centerline continues up to some point near the exit where the centerline velocity stays higher than the surface, just before the entire block travels uniformly and exits the roll gap in a horizontal direction. Flanagan et al. [8] showed the regions of constant velocity at the sheet's surface, or centre, coincide with zero plastic-equivalent-strain-rate regions where there is no local plastic deformation. While this velocity prediction is suggestive, more investigation is required to determine the effect of velocities on strain and strain rate profiles, which are critical for studying texture evolution, particularly in hot rolling.

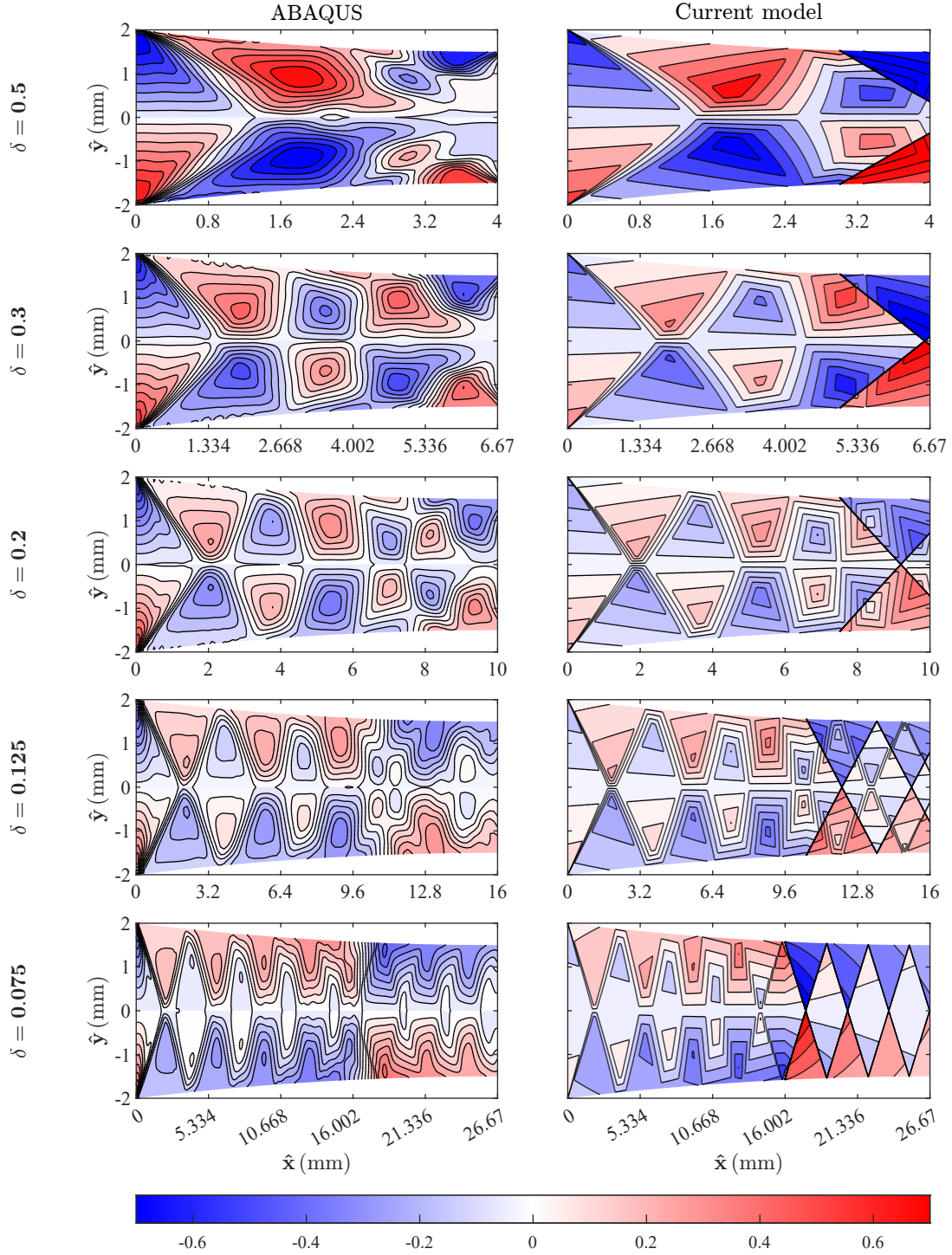


Figure 5: Comparison of shear stress results from the current model (equation (53b)) (right panel) and FE simulations [8] (left panel) for varying δ values. Results are shown in dimensionless form, i.e. scaled with $\hat{\kappa}$, the yield stress in shear. Parameters used are $(\hat{h}_0, r, \mu, \hat{\kappa}) = (2 \text{ mm}, 25\%, 0.1, 288.67 \text{ MPa})$, except $\delta = 0.5$ which uses $\mu = 0.25$ and $\delta = 0.3$ which uses $\mu = 0.15$.

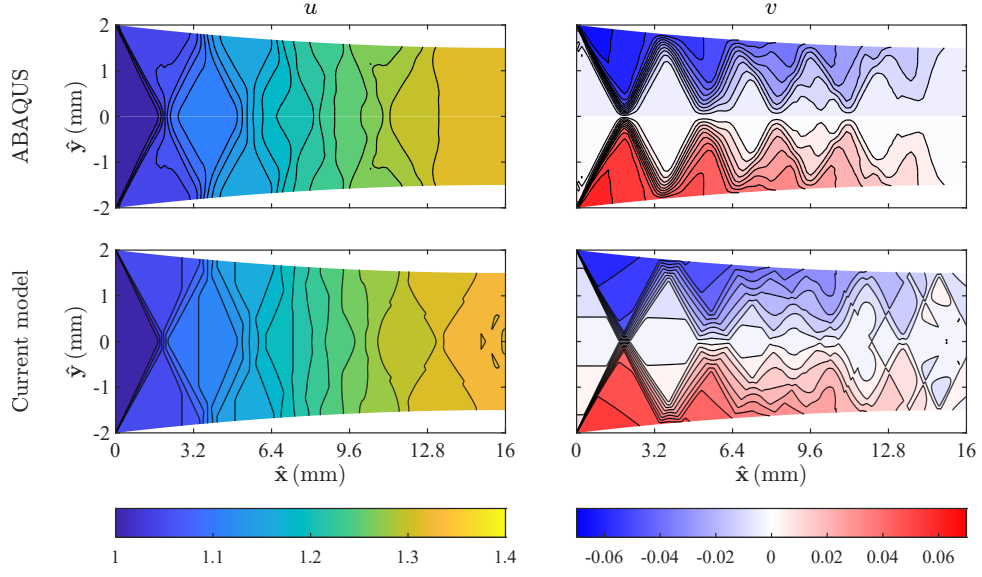


Figure 6: Comparison of velocities from the current model (equation (58)) (top row) with FE simulations [8] (bottom row) for $\delta = 0.125$. Left: contour plots of horizontal velocity, right: contour plots of vertical velocity. Results are shown in dimensionless form, i.e. scaled with \bar{U}_0 , the entrance velocity. The other parameters used are $(\hat{h}_0, r, \mu, \hat{\kappa}) = (2 \text{ mm}, 25\%, 0.1, 288.67 \text{ MPa})$

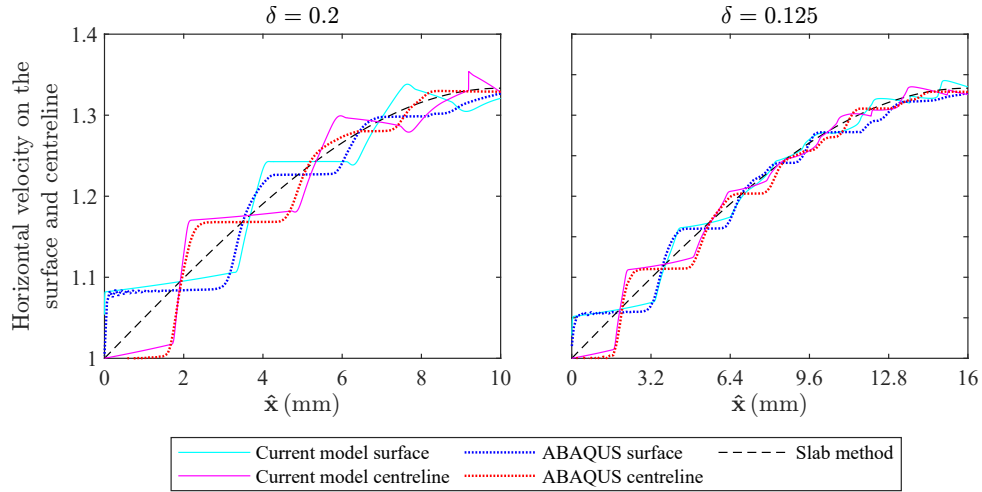


Figure 7: Plots of horizontal velocity u on the roll surface and along the centreline, plotted as functions of distance through the roll gap, for $\delta = 0.2$ (left) and $\delta = 0.125$ (right). Results are shown in dimensionless form, i.e. scaled with U_0 , the entrance velocity. Other parameters used are $(\hat{h}_0, r, \mu, \hat{\kappa}) = (2 \text{ mm}, 25\%, 0.1, 288.67 \text{ MPa})$.

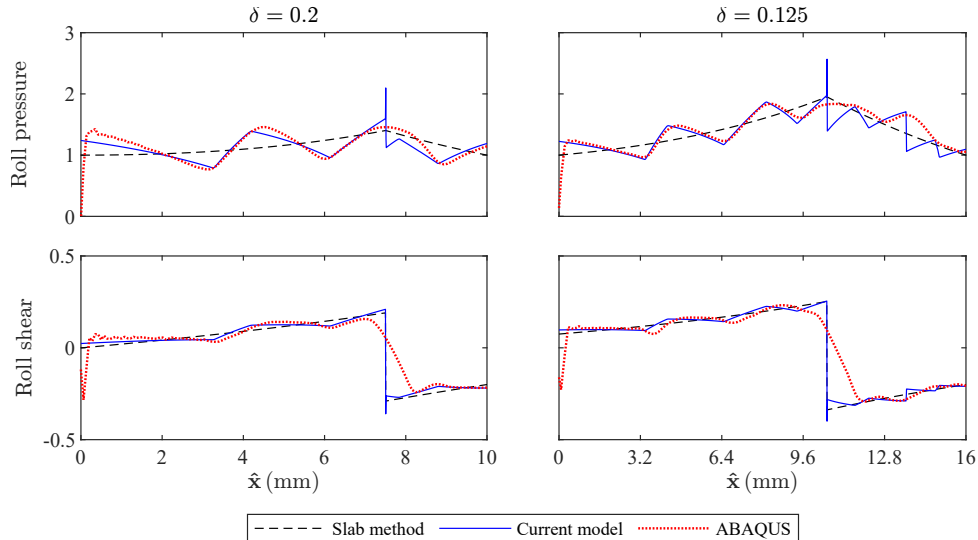


Figure 8: Plots of p (top) and σ_{xy} (bottom) on the roll surface, plotted as a function of distance through the roll gap, for $\delta = 0.2$ (left) and $\delta = 0.125$ (right). Results are shown in dimensionless form, i.e. scaled with $\hat{\kappa}$, the yield stress in shear. Other parameters used are $(\hat{h}_0, r, \mu, \hat{\kappa}) = (2 \text{ mm}, 25\%, 0.1, 288.67 \text{ MPa})$.

5.2 Comparison to slab analysis

Since slab analysis is not intended to give through-thickness information, it would be unfair to compare the results above with the slab method. Instead, here we use the stress fields on the roll surface to compare the distribution of roll pressure and roll shear between FE, slab method, and the current model. Results for two aspect ratios are plotted in Figure 8. The roll pressure marked as the “slab method” is calculated using the leading-order pressure equation (54), and the “current model” roll pressure curve is from equation (53a). For roll shear, the “slab method” curve is $y dp^{(0)}/dz$, and the correction $O(\delta^2)$ from equation $\sigma_{xy}^{(2)} \mp \beta p^{(1)} = 0$ at $y = h$ is added to this term to find the “current model” roll shear curve.

The mathematical model accurately captures the oscillations in roll pressure observed in the FE data by incorporating a correction term of magnitude δ . For short roll-gap lengths, this correction is not necessarily small, and in fact, the successive pressure peaks completely overcome the classic slab method pressure hill profile, as was observed experimentally by Al-Salehi et al. [21]. These deviations are unrelated to elastic deformation, roll flattening, or hardening, as those effects are not included here. As the sheet length increases, the stress oscillations become small fluctuations to the pressure hill. These oscillations are averaged out when integrating the roll pressure and shear over the whole roll surface to produce the roll force and roll torque; this is why both roll force and roll torque are poor measures for the accuracy of a rolling simulation [8], and why classical slab methods produce reasonable predictions for the total roll force and roll torque.

When considering roll shear, the current model prediction is identical to the slab method to the first-order correction on the surface (see equations (53b) and (56)). However, incorporating the correction of $O(\delta^2)$ on the surface accounts for the oscillations detected in the simulation, and this is what is plotted as “Current model” roll shear in Figure 8. The number of local peaks increases for longer sheet lengths, as also seen in the shear lobe pattern in Figure 5. As mentioned in the previous section, the observed discontinuity on the surface at the neutral point is an inevitable consequence of slipping Coulomb friction, while the FE simulation varies smoothly due to a small zone of sticking friction. This could be improved in future by incorporating sticking friction in the asymptotic model, although a more rigorous study would be required also incorporating elasticity, as the friction rule alone is not solely responsible for the behaviour around the neutral point [8, 14]. Such alternative friction treatments are beyond the scope of the present study. Also, the sudden changes observed near the entrance in the FE roll pressure and roll shear results are attributable to elastic deformation, which is not accounted for in the current model.

5.3 Comparison with a work-hardening FE simulation

In the previous sections, the current mathematical model was extensively verified against FE simulations which used a non-hardening material model, where the yield stress was kept fixed at $\hat{\kappa} = 288.67 \text{ MPa}$.

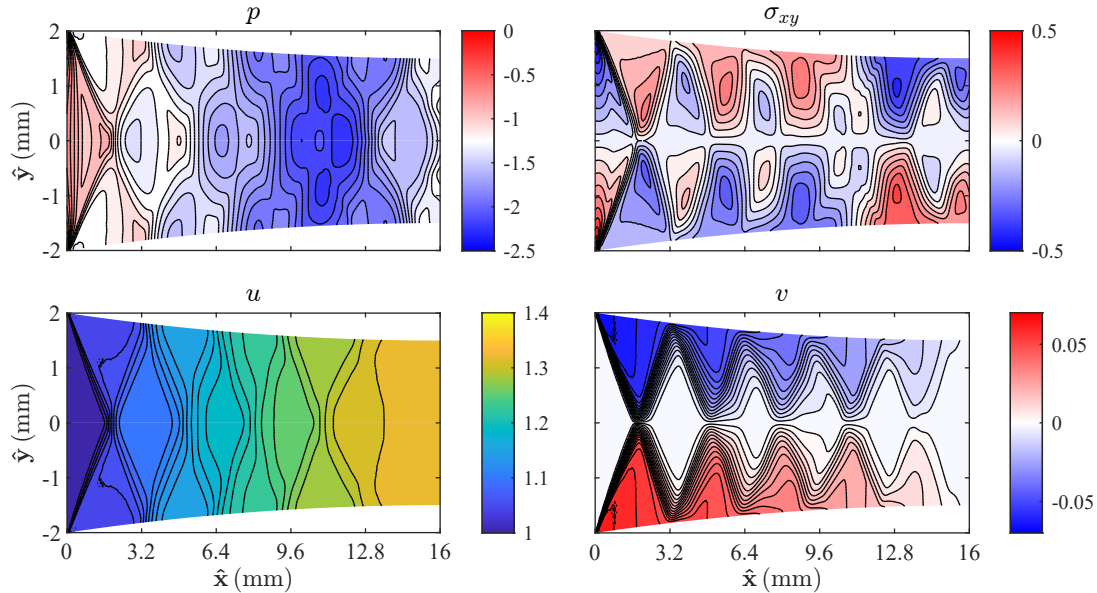


Figure 9: Contour plots of FE results [8] for $\delta = 0.125$. Material is hardened with the initial yield stress $\hat{\kappa} = 275.51$ MPa increasing to 324.29 MPa at a true plastic strain of 0.4 as a result of strain hardening. Results are scaled with the initial yield stress $\hat{\kappa} = 275.51$ MPa. Other parameters used are $(\hat{h}_0, r, \mu) = (2 \text{ mm}, 25\%, 0.1)$.

Here, FE simulation results are presented for a more realistic hardening material. For this, the initial yield stress is taken to be $\hat{\kappa} = 275.51$ MPa increasing to 324.29 MPa at a true plastic strain of 0.4 as a result of strain hardening. Strain-hardening simulations were performed for the whole range of aspect ratios shown in Figure 5, and although we only present results here for $\delta = 0.125$ for brevity, these results are typical for all values of δ .

Contour plots of stress and velocity for the hardening material for $\delta = 0.125$ are shown in Figure 9. By comparison to the equivalent non-hardening results shown in Figures 4 and 6, hardening can be seen to have a negligible effect on the through-thickness oscillatory pattern, with the effect of hardening being only a progressive increase in the magnitude of stress from left to right as the workpiece passes through the roll gap.

To examine the deviation of the model when the realistic material is concerned, we now compare the current mathematical model with non-hardening material against the simulation results with hardening material. Figure 10 shows pressure and shear distribution on the sheet surface from the current model and from FE simulation. Since in the mathematical model all stresses are scaled by the yield stress $\hat{\kappa}$, the prediction depends on its magnitude. To see the effect, we compare the simulation with the mathematical model twice: once taking the stress scaling factor as the initial yield stress $\hat{\kappa} = 275.51$ MPa; and once as the average yield stress $\hat{\kappa} = 288.67$ MPa from the hardening simulation. The impact of the different stress scalings is more noticeable on the pressure rather than shear stress, and overall, the larger scaling ($\hat{\kappa} = 288.67$ MPa) results in better agreement. The agreement is understandably better at the start of the roll gap, when the sheet undergoes little hardening, and becomes progressively worse as more hardening takes place. In summary, this comparison between the hardening simulation and non-hardening model demonstrates that the stress oscillations are unaffected by the hardening characteristics, and that the existing model remains a useful predictor for hardening materials, even though it was not specifically developed for this objective. Further improvement might be achieved in future by incorporating hardening into the mathematical model.

6 Conclusion

A semi-analytic model for symmetric rolling under Coulomb friction has been presented. The semi-analytical solution was achieved via the systematic assumptions that the aspect ratio, $1/\delta$, is large, and the friction coefficient, μ , is correspondingly small, which are common in practice. A simplified material model was assumed that neglects both elasticity and work-hardening. Despite this, the model is in good

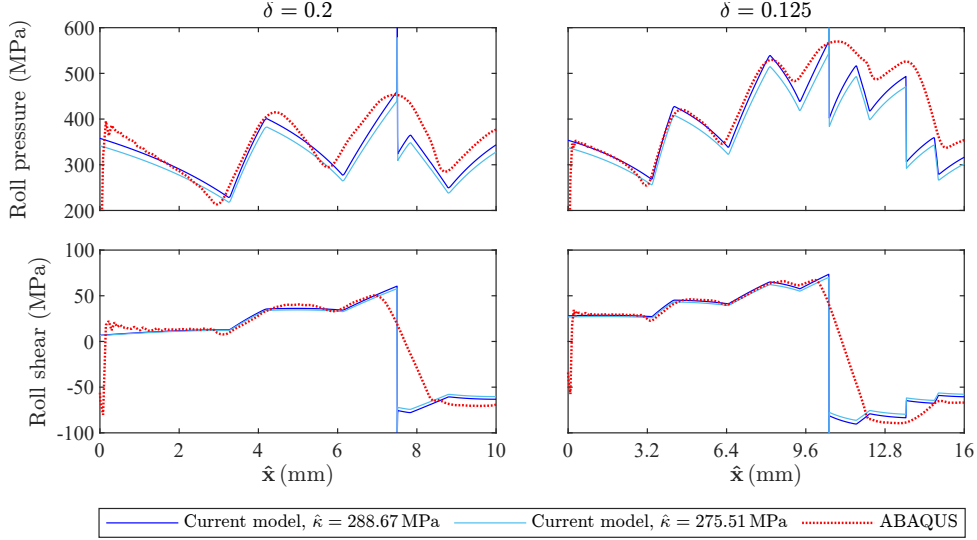


Figure 10: Plots of p (top) and σ_{xy} (bottom) on the roll surface, plotted as a function of distance through the roll gap. ABAQUS results [8] are from hardening material, with an initial yield stress of $\hat{\kappa} = 275.51$ MPa increasing to 324.29 MPa at a true plastic strain of 0.4 as a result of strain hardening. The current model is for non-hardening material with two different yield stresses $\hat{\kappa} = 288.67$ MPa and $\hat{\kappa} = 275.51$ MPa. The left panel shows results for $\delta = 0.2$. The right panel shows results for $\delta = 0.125$. Other parameters used are $(\hat{h}_0, r, \mu) = (2 \text{ mm}, 25\%, 0.1)$

agreement with FE simulations that do not make these assumptions. While the rolls were considered rigid here, the shape of the rolls in the model ($h(z)$) is arbitrary and could be iterated to include roll flattening.

Two length scales were introduced which enable the use of a multiple-scales asymptotic analysis: the large scale of the length of the roll gap, \hat{l} ; and the small length scale of the initial sheet half-thickness, \hat{h}_0 . The leading-order solution depends on the large length scale only and recreates the conventional pressure hill from slab analysis. The next-order correction is an order $O(\delta)$ smaller than the leading order, depends on both the large and small length scales, and provides a new prediction of through-thickness variation that shows an oscillatory pattern. This work is distinguished by this correction term, and generalises a previous asymptotic analysis by Minton et al. [26] that incorrectly neglected these $O(\delta)$ correction terms. It should be noted that the shear stress is zero at leading order, and so this $O(\delta)$ “correction term” actually gives the leading-order behaviour of the shear stress. The first-order correction terms reveal two sets of waves for stress and velocity distribution varying on the short length scale of the sheet thickness. These are governed by a Burger’s equation and an advection equation respectively, and can easily be solved numerically with suitable initial conditions at the roll-gap entrance. These corrections to the stress distribution have a minimal influence on the overall roll force and torque predictions, indicating that the accuracy of roll forces and torques are poor indications of the quality and accuracy of the entire simulation. Moreover, these fine details in the stress and velocity distribution will likely become significant when studying material properties, such as the hardening, development of anisotropy, or development of residual stress in the rolled sheet.

A set of rigorous FE simulations using ABAQUS/Standard were performed for steady-state conditions, as detailed by Flanagan et al. [8]. Significant work was needed for the FE simulation to be sufficiently accurate to give good agreement with the mathematical model. This highlights another use of the mathematical model presented here: it can be used to validate FE simulations. To date, the asymptotic solution and FE simulations shown here demonstrate the highest degree of agreement the authors are aware of in the literature. The solutions deviate in three places due to the simplifying assumptions of the mathematical model: the entrance and exit regions are sub-yield and are therefore governed by elasticity, which is neglected in the mathematical model; and the neutral point demonstrates sticking behaviour in the numerical simulations while only slipping friction was assumed in the mathematical model. These differences do not appear to affect either the quantitative predictions of the mathematical model elsewhere in the roll gap, nor the overall qualitative predictions of the model in general.

The mathematical model presented in this study offers a significant advantage in terms of computa-

tional efficiency compared to FE simulations. The FE simulations for $\delta = 0.125$ used in this paper took 15.89 hours CPU time to run on a standard desktop computer, making them unsuitable for optimisation and real-time control. In contrast, the unoptimised MATLAB code evaluating the new mathematical model for the same δ took 3.45 seconds CPU time to run on a standard laptop which is more than 16,000 times faster compared to FE simulation.

Further work could look at the entry and exit boundary conditions, likely by the inclusion of an elastic entrance and exit region. Similarly, including elasticity and a sticking friction model near the neutral point would smooth the shock that is seen in the mathematical model but not the FE simulations. Calculating higher-order terms, for example of $O(\delta^2)$, may or may not lead to more accurate results, and is unlikely to uncover new behaviour. It may also be interesting to consider whether more mathematical techniques investigating slow, invariant, or centre manifolds may give either more insight or further accuracy [34–36]. As mentioned above, incorporating roll flattening would allow the model to be applied to more extreme rolling cases such as foil rolling [extending 13], and would involve adding an evolution equation to the roll shape $h(x)$ which is here taken to be arbitrary but known. The assumption of symmetry could also be relaxed to enable the prediction of asymmetric rolling [extending 26], and temperature and recrystallisation effects could be included in order to model hot rolling processes. Including heating and heat flux in the model might allow the prediction of similar oscillatory patterns observed in the heat flux during rolling [42]. Another extension might be to predict the stress field in other rolling processes, such as wire rolling [43, 44]. Finally, the present model’s assumptions of perfect plasticity could be generalised to more realistic material models including strain-hardening and strain-rate-hardening, which is currently work in progress. Of course, all of these modifications would further complicate the model, making it harder to understand and interpret the fundamental mechanics; we therefore believe the present model represents a good balance between complexity and understandability, retaining most of the underlying simplicity of slab methods and introducing the wave-like behaviour needed for reasonable comparison with FE simulations.

Acknowledgements

ME gratefully acknowledges the support of a University of Warwick Chancellor’s Scholarship. EJB is grateful for the UKRI Future Leaders’ Fellowship funding (MR/V02261X/1) supporting this work. FF is supported by Science Foundation Ireland Grant #18/CRT/6049. DOK is grateful for funding from the Science Foundation Ireland (21/FFP-P/10160). ANOC is supported by the European Union, Science Foundation of Ireland and Lero, the Science Foundation Ireland Research Centre for Software, grants #101028291 #13/RC/2094 and #SOWP2-TP0023, respectively. For the purpose of open access, the authors have applied a Creative Commons Attribution (CC BY) licence to any Author Accepted Manuscript version arising from this submission.

A preliminary version of some parts of this work was presented at the 14th International Conference on the Technology of Plasticity, Mandelieu, France, September 2023 [45].

A Solving for the second-order stresses

In this appendix, The solution is continued to this order of correction with the goal of finding the unknown parameters $A(\xi, z)$ and $D(z)$ from the previous order. From the yield function (16a), at $O(\delta^2)$, and substituting the known variables from the previous orders, we find that

$$\sigma_{xx}^{(2)} = -p^{(2)} - \frac{1}{2}\sigma_{xy}^{(1)2} \quad \text{and} \quad \sigma_{yy}^{(2)} = -p^{(2)} + \frac{1}{2}\sigma_{xy}^{(1)2}. \quad (\text{A.1})$$

At $O(\delta^2)$, the momentum equations (16b) and (16c) are

$$\frac{\partial \sigma_{xx}^{(1)}}{\partial z} + \frac{1}{h} \frac{\partial \sigma_{xx}^{(2)}}{\partial n} + \frac{\partial \sigma_{xy}^{(2)}}{\partial y} = 0 \quad \text{and} \quad \frac{\partial \sigma_{yy}^{(2)}}{\partial y} + \frac{\partial \sigma_{xy}^{(1)}}{\partial z} + \frac{1}{h} \frac{\partial \sigma_{xy}^{(2)}}{\partial n} = 0. \quad (\text{A.2})$$

By substituting in $\sigma_{xx}^{(2)}$ and $\sigma_{yy}^{(2)}$ from equation (A.1), and $\sigma_{xx}^{(1)}$ from (23), we have,

$$\frac{\partial \sigma_{xy}^{(2)}}{\partial y} - \frac{1}{h} \frac{\partial p^{(2)}}{\partial n} = \frac{\partial p^{(1)}}{\partial z} + \frac{1}{2h} \frac{\partial \sigma_{xy}^{(1)2}}{\partial n} \quad \text{and} \quad \frac{\partial p^{(2)}}{\partial y} - \frac{1}{h} \frac{\partial \sigma_{xy}^{(2)}}{\partial n} = \frac{\partial \sigma_{xy}^{(1)}}{\partial z} + \frac{1}{2} \frac{\partial \sigma_{xy}^{(1)2}}{\partial y}. \quad (\text{A.3})$$

These two equations give wave equations for $p^{(2)}$ and $\sigma_{xy}^{(2)}$, forced by $p^{(1)}$ and $\sigma_{xy}^{(1)}$. By substituting $p^{(1)}$ and $\sigma_{xy}^{(1)}$ from equation (25) into (A.3), we arrive at

$$\begin{aligned} \frac{\partial \sigma_{xy}^{(2)}}{\partial y} - \frac{1}{h(z)} \frac{\partial p^{(2)}}{\partial n} &= \left[\frac{\partial A}{\partial z} \left(n + \frac{y}{h} \right) + \frac{\partial A}{\partial z} \left(n - \frac{y}{h} \right) \right] - \frac{dD(z)}{dz} \\ &+ \frac{1}{2h} \frac{\partial}{\partial n} \left[A \left(n + \frac{y}{h} \right)^2 + A \left(n - \frac{y}{h} \right)^2 - 2A \left(n + \frac{y}{h} \right) A \left(n - \frac{y}{h} \right) \right] \\ &+ \frac{y}{h} \left[A' \left(n + \frac{y}{h} \right) - A' \left(n - \frac{y}{h} \right) \right] \left(\frac{dp^{(0)}}{dz} - \frac{dh/dz}{h} \right) \end{aligned} \quad (\text{A.4a})$$

$$\begin{aligned} \frac{\partial p^{(2)}}{\partial y} - \frac{1}{h} \frac{\partial \sigma_{xy}^{(2)}}{\partial n} &= \left[\frac{\partial A}{\partial z} \left(n + \frac{y}{h} \right) - \frac{\partial A}{\partial z} \left(n - \frac{y}{h} \right) \right] \\ &+ \frac{1}{2} \frac{\partial}{\partial y} \left[A \left(n + \frac{y}{h} \right)^2 + A \left(n - \frac{y}{h} \right)^2 - 2A \left(n + \frac{y}{h} \right) A \left(n - \frac{y}{h} \right) \right] \\ &+ \frac{y}{h} \left[A' \left(n + \frac{y}{h} \right) + A' \left(n - \frac{y}{h} \right) \right] \left(\frac{dp^{(0)}}{dz} - \frac{dh/dz}{h} \right) \\ &+ y \left(\left(\frac{dp^{(0)}}{dz} \right)^2 + \frac{\partial^2 p^{(0)}}{\partial z^2} \right) + \frac{dp^{(0)}}{dz} \left[A \left(n + \frac{y}{h} \right) - A \left(n - \frac{y}{h} \right) \right], \end{aligned} \quad (\text{A.4b})$$

where prime denoting $\partial/\partial\xi$, and $A(n \pm (y/h), z)$ is abbreviated to $A(n \pm (y/h))$ for brevity while the dependence on z is still acknowledged.

In principle, $p^{(2)}$ can be eliminated from (A.4b) and the resulting second-order differential equation can be solved for $\sigma_{xy}^{(2)}$, and vice versa. However, we found it more manageable to solve as a system of two coupled equations, by finding particular integrals for each of the forcing terms on the right-hand-side. Ultimately, we find the final solution for $\sigma_{xy}^{(2)}$ and $p^{(2)}$ as

$$\begin{aligned} \sigma_{xy}^{(2)} &= M \left(n + \frac{y}{h} \right) - M \left(n - \frac{y}{h} \right) + y \left[\frac{\partial A}{\partial z} \left(n + \frac{y}{h} \right) + \frac{\partial A}{\partial z} \left(n - \frac{y}{h} \right) \right] \\ &+ \frac{y^2}{2h} \left(\frac{dp^{(0)}}{dz} - \frac{dh/dz}{h} \right) \left[A' \left(n + \frac{y}{h} \right) - A' \left(n - \frac{y}{h} \right) \right] + \frac{y}{2} \frac{dp^{(0)}}{dz} \left[A \left(n + \frac{y}{h} \right) + A \left(n - \frac{y}{h} \right) \right] \\ &+ \frac{1}{2} \left[A' \left(n + \frac{y}{h} \right) A^\wedge \left(n - \frac{y}{h} \right) - A^\wedge \left(n + \frac{y}{h} \right) A' \left(n - \frac{y}{h} \right) \right] \\ &- \frac{h}{2} \frac{dp^{(0)}}{dz} \left[A^\wedge \left(n + \frac{y}{h} \right) - A^\wedge \left(n - \frac{y}{h} \right) \right] + \frac{y}{2h} \frac{\partial}{\partial n} \left[A \left(n + \frac{y}{h} \right)^2 + A \left(n - \frac{y}{h} \right)^2 \right] - y \frac{dD(z)}{dz}, \end{aligned} \quad (\text{A.5a})$$

$$\begin{aligned} p^{(2)} &= M \left(n + \frac{y}{h} \right) + M \left(n - \frac{y}{h} \right) + y \left[\frac{\partial A}{\partial z} \left(n + \frac{y}{h} \right) - \frac{\partial A}{\partial z} \left(n - \frac{y}{h} \right) \right] \\ &+ \frac{y^2}{2h} \left(\frac{dp^{(0)}}{dz} - \frac{dh/dz}{h} \right) \left[A' \left(n + \frac{y}{h} \right) + A' \left(n - \frac{y}{h} \right) \right] + \frac{y}{2} \frac{dp^{(0)}}{dz} \left[A \left(n + \frac{y}{h} \right) - A \left(n - \frac{y}{h} \right) \right] \\ &+ \frac{1}{2} \left[A' \left(n + \frac{y}{h} \right) A^\wedge \left(n - \frac{y}{h} \right) + A^\wedge \left(n + \frac{y}{h} \right) A' \left(n - \frac{y}{h} \right) \right] \\ &+ \frac{y}{2h} \frac{\partial}{\partial n} \left[A \left(n + \frac{y}{h} \right)^2 - A \left(n - \frac{y}{h} \right)^2 \right] + \frac{y^2}{2} \left(\frac{d^2 p^{(0)}(z)}{dz^2} + \left(\frac{dp^{(0)}(z)}{dz} \right)^2 \right), \end{aligned} \quad (\text{A.5b})$$

where the term $M(n + (y/h)) - M(n - (y/h))$ represents the complementary solution, which is an as-yet-unknown wave, and A^\wedge is the integral of A such that $A^\wedge' = A$.

Substituting this solution into the friction equation at this order, $\sigma_{xy}^{(2)} \mp \beta p^{(1)} = 0$, results in

$$\begin{aligned}
M(n+1, z) - M(n-1, z) + h \left[\frac{\partial A(n+1, z)}{\partial z} + \frac{\partial A(n-1, z)}{\partial z} \right] \\
+ \frac{h}{2} \left(\frac{dp^{(0)}}{dz} - \frac{dh/dz}{z} \right) [A'(n+1, z) - A'(n-1, z)] + \frac{h}{2} \frac{dp^{(0)}}{dz} [A(n+1, z) + A(n-1, z)] \\
+ \frac{1}{2} [A'(n+1, z)A^\wedge(n-1, z) - A'(n-1, z)A^\wedge(n+1, z)] - \frac{h}{2} \frac{dp^{(0)}}{dz} [A^\wedge(n+1, z) - A^\wedge(n-1, z)] \\
+ \frac{1}{2} \frac{\partial}{\partial n} [A(n+1, z)^2 + A(n-1, z)^2] - h \frac{\partial D(z)}{\partial z} \mp \beta [A(n+1, z) + A(n-1, z) + D(z)] = 0.
\end{aligned} \tag{A.6}$$

This equation can be significantly simplified by using the condition (28), to give

$$\begin{aligned}
2h \frac{\partial A(n+1, z)}{\partial z} + \frac{\partial}{\partial n} (A(n+1, z)^2) + \left(h \frac{dp^{(0)}}{dz} \mp 2\beta \right) A(n+1, z) \\
- h \frac{dD(z)}{dz} \mp \beta D(z) = -[M(n+1, z) - M(n-1, z)].
\end{aligned} \tag{A.7}$$

Where the term $M(n+1, z) - M(n-1, z)$ is the wave-equation solution for $\sigma_{xy}^{(2)}$ to the homogeneous version of the coupled problem in (A.3). We do not need to calculate M , however as by the same secularity argument used for A at first order, we require that M is bounded in n , and consequently, we require the right-hand side of equation (A.7) to be zero. The resulting equation is quoted in (33).

B Burger's equation

The evolutionary equation (A.7) for $A(\xi, z)$ was simplified in Section 3.1.3 to equation (35), which is

$$2h \frac{\partial A(\xi, z)}{\partial z} + \frac{\partial}{\partial \xi} (A(\xi, z)^2) + \left(h \frac{dp^{(0)}}{dz} \mp 2\beta \right) A(\xi, z) = 0. \tag{B.1}$$

The factor $h dp^{(0)}/dz$ in (B.1) can be replaced with its equivalent in equation (30). Then, equation (B.1) becomes

$$\frac{\partial A(\xi, z)}{\partial z} + \frac{1}{2h} \frac{\partial}{\partial \xi} (A(\xi, z)^2) - \left(\mp \frac{\beta}{2h} (p^{(0)} - 1) - \frac{dh/dz}{h} \right) A(\xi, z) = 0. \tag{B.2}$$

Our solution methodology for the partial differential equation in (B.2) will involve combining the first and third terms into a single z -derivative. To this end, we first rewrite the factor multiplying A as a z -derivative by defining,

$$\alpha_1 = \exp \left\{ \int_0^z \left(\mp \frac{\beta}{2h(\tilde{z})} (p^{(0)}(\tilde{z}) - 1) \right) d\tilde{z} \right\}, \tag{B.3}$$

so that,

$$\exp \left\{ \int_0^z \left(\mp \frac{\beta}{2h(\tilde{z})} (p^{(0)}(\tilde{z}) - 1) - \frac{dh/dz}{h(\tilde{z})} \right) d\tilde{z} \right\} = \frac{\alpha_1}{h}. \tag{B.4}$$

When differentiating both sides with respect to z , we then recover

$$\left(\mp \frac{\beta}{2h} (p^{(0)} - 1) - \frac{dh/dz}{h} \right) = \frac{\partial}{\partial z} (\alpha_1/h). \tag{B.5}$$

Replacing this into the original equation (B.2), this equation can be rewritten as

$$\frac{\partial A(\xi)}{\partial z} - \frac{\partial}{\partial z} (\alpha_1/h) A(\xi) + \frac{1}{2h} \frac{\partial}{\partial \xi} (A(\xi)^2) = 0. \tag{B.6}$$

By dividing the equation by α_1/h , then, the first two terms are z derivative of $\frac{A(\xi)}{(\alpha_1/h)}$. Thus,

$$\frac{\partial}{\partial z} \left(\frac{A(\xi)}{(\alpha_1/h)} \right) + \frac{\alpha_1}{2h^2} \frac{\partial}{\partial \xi} \left(\left(\frac{A(\xi)}{(\alpha_1/h)} \right)^2 \right) = 0. \tag{B.7}$$

Finally, with the following change of variable, Burger's equation is obtained,

$$T = \int^z \frac{\alpha_1}{h(\bar{z})^2} d\bar{z} \quad \text{and} \quad \omega(\xi, T(z)) = \frac{A(\xi, z)}{(\alpha_1/h)} \quad (\text{B.8a})$$

$$\Rightarrow \quad \frac{\partial}{\partial T}(\omega) + \frac{1}{2} \frac{\partial}{\partial \xi}(\omega^2) = 0. \quad (\text{B.8b})$$

C The inner solution around the neutral point

As described in Section 3.1.4, in order to avoid a through-thickness discontinuity in $\sigma_{xy}^{(1)}$ as a result of $y dp^{(0)}/dz$ term (see change in the sign of shear stress through a vertical line at the neutral point in Figure 3), we here investigate carefully an inner region close to the neutral point. We introduce a new coordinate X measuring distance near the neutral point,

$$z = z_N + \delta X, \quad (\text{C.1})$$

where z_N is the location of the neutral point obtained from the leading-order solution. We allow for an $O(\delta)$ correction to the location of the neutral point, by considering the neutral point to actually occur at $X = X_N$, where X_N is the correction.

From (C.1), it can be seen that X varies on the same length scale as the workpiece thickness, and so is comparable to the original x coordinate in (7a). Within the inner region, there is only one length scale, and so we do not need the multiple-scales variables z and n ; stresses are only functions of X and y . Therefore, the governing equations are

$$\frac{\partial \sigma_{xx_{\text{inner}}}}{\partial X} + \frac{\partial \sigma_{xy_{\text{inner}}}}{\partial y} = 0 \quad (\text{C.2a})$$

$$\frac{\partial \sigma_{yy_{\text{inner}}}}{\partial y} + \frac{\partial \sigma_{xy_{\text{inner}}}}{\partial X} = 0 \quad (\text{C.2b})$$

$$\frac{1}{4} (\sigma_{xx_{\text{inner}}} - \sigma_{yy_{\text{inner}}})^2 + (\sigma_{xy_{\text{inner}}})^2 = 1 \quad (\text{C.2c})$$

$$\begin{aligned} \delta \frac{dh}{dz} (\sigma_{yy_{\text{inner}}} - \sigma_{xx_{\text{inner}}}) + \left(1 - \delta^2 \left(\frac{dh}{dz} \right)^2 \right) \sigma_{xy_{\text{inner}}} \\ = \mp \delta \beta \left[\sigma_{yy_{\text{inner}}} - 2\delta \frac{dh}{dz} \sigma_{xy_{\text{inner}}} + \delta^2 \left(\frac{dh}{dz} \right)^2 \sigma_{xx_{\text{inner}}} \right] \quad \text{at } y = h(z). \end{aligned} \quad (\text{C.2d})$$

The subscript ‘‘inner’’ indicates that the parameters associated with it pertain to the inner region and possess values that are different from those in the outer region. At the leading order, $\sigma_{xy_{\text{inner}}}^{(0)}$ is zero similar to the outer region. From momentum conservation (C.2a) and (C.2b) together with the yield function (C.2c), it becomes evident that $\sigma_{xx_{\text{inner}}}^{(0)}$, $\sigma_{yy_{\text{inner}}}^{(0)}$ and $p_{\text{inner}}^{(0)}$ are all independent of X and y , and are therefore constants,

$$\sigma_{xx_{\text{inner}}}^{(0)} = 1 - p_{\text{inner}}^{(0)} \quad \text{and} \quad \sigma_{yy_{\text{inner}}}^{(0)} = -1 - p_{\text{inner}}^{(0)}. \quad (\text{C.3})$$

At $O(\delta)$, the yield condition (C.2c) becomes

$$\sigma_{xx_{\text{inner}}}^{(1)} - \sigma_{yy_{\text{inner}}}^{(1)} = 0 \quad \Rightarrow \quad \sigma_{xx_{\text{inner}}}^{(1)} = \sigma_{yy_{\text{inner}}}^{(1)} = -p_{\text{inner}}^{(1)}. \quad (\text{C.4})$$

Substituting this into the momentum conservation equations (C.2a) and (C.2b), the following equations are obtained, respectively

$$-\frac{\partial p_{\text{inner}}^{(1)}}{\partial X} + \frac{\partial \sigma_{xy_{\text{inner}}}^{(1)}}{\partial y} = 0, \quad -\frac{\partial p_{\text{inner}}^{(1)}}{\partial y} + \frac{\partial \sigma_{xy_{\text{inner}}}^{(1)}}{\partial X} = 0. \quad (\text{C.5})$$

The solution that satisfies the above differential equations is the wave-like solution

$$p_{\text{inner}}^{(1)} = G \left(\frac{X}{h_N} + \frac{y}{h_N} \right) + G \left(\frac{X}{h_N} - \frac{y}{h_N} \right), \quad (\text{C.6a})$$

$$\sigma_{xy_{\text{inner}}}^{(1)} = G \left(\frac{X}{h_N} + \frac{y}{h_N} \right) - G \left(\frac{X}{h_N} - \frac{y}{h_N} \right), \quad (\text{C.6b})$$

where $h_N = h(z_N)$ is the half-thickness at the unperturbed neutral point and G is an as-yet-unknown wave. Substituting $\sigma_{xy\text{inner}}^{(1)}$ into the Coulomb friction equation (C.2d) at $O(\delta)$ gives a periodicity constraint on G that

$$-2 \frac{dh}{dz} \Big|_{z=z_N} + \left[G \left(\frac{X}{h_N} + 1 \right) - G \left(\frac{X}{h_N} - 1 \right) \right] \mp \beta(1 + p_{\text{inner}}^{(0)}) = 0, \quad (\text{C.7})$$

where $\mp = \text{sgn}(X - X_N)$.

This inner solution derived above should match with the previously derived solutions both to the left and to the right of the neutral point, as $|X| \rightarrow \infty$. Let us write $p^{(-)}$ and $p^{(+)}$ for the pressure calculated to the left ($-$) and to the right ($+$) of the neutral point, and similarly for $\sigma_{xy}^{(\mp)}$. Then the inner solution should match with the expansions of these outer solutions when expanded in terms of X , so that, as $X \rightarrow \pm\infty$, we should have

$$\begin{aligned} p &= p^{(0\mp)}(y, z_N + \delta X) + \delta p^{(1\mp)}(n_N + X/h_N + O(\delta), y, z_N + \delta X) + O(\delta^2) \\ &= p^{(0)}(z_N) + \delta \left[A^{(\mp)} \left(n_N + \frac{X}{h_N} + \frac{y}{h_N}, z_N \right) + A^{(\mp)} \left(n_N + \frac{X}{h_N} - \frac{y}{h_N}, z_N \right) + X \frac{dp^{(0\mp)}(z_N)}{dz} \right] + O(\delta^2), \end{aligned} \quad (\text{C.8a})$$

$$\begin{aligned} \sigma_{xy} &= \sigma_{xy}^{(1\mp)}(n_N + X/h_N + O(\delta), y, z_N + \delta X) + O(\delta^2) \\ &= \delta \left[A^{(\mp)} \left(n_N + \frac{X}{h_N} + \frac{y}{h_N}, z_N \right) - A^{(\mp)} \left(n_N + \frac{X}{h_N} - \frac{y}{h_N}, z_N \right) + y \frac{dp^{(0\mp)}(z_N)}{dz} \right] + O(\delta^2), \end{aligned} \quad (\text{C.8b})$$

where $p^{(1\mp)}$ and $\sigma_{xy}^{(1\mp)}$ are taken from equation (25), $p^{(0\mp)}$ satisfies (30), and $A^{(\mp)}(\xi, z)$ is the function $A(\xi, z)$ used in the outer solution to either the left ($-$) or the right ($+$) of the neutral point. The main reason for this appendix is to calculate the correct link between $A^{(+)}(\xi, z)$ and $A^{(-)}(\xi, z)$. Note that $p^{(0+)}(z_N) = p^{(0-)}(z_N)$, as this is how the neutral point z_N is chosen, but that $dp^{(0+)}/dz \neq dp^{(0-)}/dz$ at $z = z_N$ (see equation 30).

At leading order, equation (C.8) gives $p_{\text{inner}}^{(0)} = p^{(0)}(z_N)$, as might have been expected, and confirms that $\sigma_{xy\text{inner}}^{(0)} = 0$.

We may exactly match $\sigma_{xy\text{inner}}^{(1)}$ and $p_{\text{inner}}^{(1)}$ given in equation (C.6) with the $O(\delta)$ part of equation (C.8) with $(\mp) = (-)$ by taking

$$G(\xi) = A^{(-)}(n_N + \xi, z_N) + \frac{h_N}{2} \xi \frac{dp^{(0-)}}{dz} \Big|_{z=z_N} \quad \text{for} \quad \xi < \frac{X_N}{h_N} + 1. \quad (\text{C.9})$$

Since $A^{(-)}(n+1, z) = A^{(-)}(n-1, z)$ owing to (28), and since $p^{(0-)}$ satisfies (25), this solution for $G(\xi)$ exactly satisfies the periodicity constraint (C.7) with $\mp = -$. However, $\mp = -$ is only the correct choice for $X < X_N$, and consequently (C.7) is only satisfied by this choice of $G(\xi)$ for $\xi < X_N/h_N + 1$, as indicated in (C.9).

Similarly, we may exactly match $\sigma_{xy\text{inner}}^{(1)}$ and $p_{\text{inner}}^{(1)}$ given in equation (C.6) with the $O(\delta)$ part of equation (C.8) with $(\mp) = (+)$ by taking

$$G(\xi) = A^{(+)}(n_N + \xi, z_N) + \frac{h_N}{2} \xi \frac{dp^{(0+)}}{dz} \Big|_{z=z_N} \quad \text{for} \quad \xi > \frac{X_N}{h_N} - 1. \quad (\text{C.10})$$

As before, since $A^{(+)}(n+1, z) = A^{(+)}(n-1, z)$ owing to (28), this solution for $G(\xi)$ exactly satisfies the periodicity constraint (C.7) with $\mp = +$. However, $\mp = +$ is only the correct choice for $X > X_N$, and consequently (C.7) is only satisfied by this choice of $G(\xi)$ for $\xi > X_N/h_N - 1$, as indicated in (C.10).

In order to satisfy both (C.9) and (C.10), for $X_N/h_N - 1 < \xi < X_N/h_N + 1$ we must have

$$G(\xi) = A^{(-)}(n_N + \xi, z_N) + \frac{h_N}{2} \xi \frac{dp^{(0-)}}{dz} \Big|_{z=z_N} = A^{(+)}(n_N + \xi, z_N) + \frac{h_N}{2} \xi \frac{dp^{(0+)}}{dz} \Big|_{z=z_N} \quad (\text{C.11a})$$

$$\begin{aligned} \Rightarrow \quad A^{(+)}(n_N + \xi, z_N) &= A^{(-)}(n_N + \xi, z_N) + \frac{h_N}{2} \xi \left[\frac{dp^{(0-)}}{dz} \Big|_{z=z_N} - \frac{dp^{(0+)}}{dz} \Big|_{z=z_N} \right] \\ &= A^{(-)}(n_N + \xi, z_N) + 2\beta\xi(1 + p^{(0)}(z_N)). \end{aligned} \quad (\text{C.11b})$$

In the outer region, the condition (28) results in $\int A^{(\mp)}(\xi) d\xi = 0$. Therefore,

$$0 = \int A^{(+)}(\xi) d\xi = \int_{\frac{x_N}{h_N}-1}^{\frac{x_N}{h_N}+1} A^{(-)}(n_N + \xi, z_N) d\xi + \int_{\frac{x_N}{h_N}-1}^{\frac{x_N}{h_N}+1} \beta\xi \left(p^{(0)}(z_N) + 1 \right) d\xi = 2\beta \left(p^{(0)}(z_N) + 1 \right) \frac{X_N}{h_N}. \quad (\text{C.12})$$

In order for this equality to be satisfied, we must take $X_N = 0$. This means there is no $O(\delta)$ correction to the location of the neutral point, and the neutral point is located at $z = z_N$, found from equation (30) for $p^{(0)}$ in the outer region. Equation (C.11b) thus gives the connection between the solutions to the left and right of the neutral point, which is the solution given in (38) in the main text.

D Solving for the second-order velocities

In this appendix, we solve equations (49) in the main text, which describe the velocity at $O(\delta^2)$. This does not completely resolve the velocity, as it will be determined only up to an unknown function $N(\xi, z)$ which would be determined at the next order, $O(\delta^3)$. However, requiring that $v^{(2)}$ remains bounded, and in particular that it remains asymptotically smaller than the previous term $v^{(1)}$, does give us a secularity condition for the previously unknown function $B(\xi, z)$ which occurs in $v^{(1)}$, and that allows us to completely determine $v^{(1)}$.

We begin with equation (49), given by

$$\frac{\partial v^{(2)}}{\partial y} + \frac{1}{h} \frac{\partial u^{(2)}}{\partial n} = - \frac{\partial u^{(1)}}{\partial z} \quad (\text{D.1a})$$

$$\frac{\partial u^{(2)}}{\partial y} + \frac{1}{h} \frac{\partial v^{(2)}}{\partial n} = - \frac{\partial v^{(1)}}{\partial z} + 2\lambda^{(1)} \sigma_{xy}^{(1)}. \quad (\text{D.1b})$$

Substituting the solutions obtained for $u^{(1)}$, $v^{(1)}$, $\lambda^{(1)}$, and $\sigma_{xy}^{(1)}$ from equation (45), (46), and (25b) into (D.1) yields

$$\begin{aligned} \frac{\partial u^{(2)}}{\partial y} + \frac{1}{h} \frac{\partial v^{(2)}}{\partial n} = & \left[\frac{\partial B}{\partial z} \left(n + \frac{y}{h} \right) - \frac{\partial B}{\partial z} \left(n - \frac{y}{h} \right) \right] - 2 \frac{dh/dz}{h^2} \left[A \left(n + \frac{y}{h} \right) - A \left(n - \frac{y}{h} \right) \right] \\ & + y \left(\frac{2}{h} \frac{dp^{(0)}}{dz} - \frac{dh/dz}{h^2} \right) \left[B' \left(n + \frac{y}{h} \right) + B' \left(n - \frac{y}{h} \right) \right] \\ & + \frac{2}{h} \left[A \left(n + \frac{y}{h} \right) - A \left(n - \frac{y}{h} \right) \right] \left[B' \left(n + \frac{y}{h} \right) + B' \left(n - \frac{y}{h} \right) \right] \\ & - y \left(\frac{h(d^2h/dz^2) - 2(dh/dz)^2}{h^3} + 2 \frac{dh/dz}{h^2} \frac{dp^{(0)}}{dz} \right) \end{aligned} \quad (\text{D.2a})$$

$$\frac{\partial v^{(2)}}{\partial y} + \frac{1}{h} \frac{\partial u^{(2)}}{\partial n} = - \left[\frac{\partial B}{\partial z} \left(n + \frac{y}{h} \right) + \frac{\partial B}{\partial z} \left(n - \frac{y}{h} \right) \right] + y \frac{dh/dz}{h^2} \left[B' \left(n + \frac{y}{h} \right) - B' \left(n - \frac{y}{h} \right) \right], \quad (\text{D.2b})$$

where $A(n \pm (y/h), z)$ and $B(n \pm (y/h), z)$ are abbreviated to $A(n \pm (y/h))$ and $B(n \pm (y/h))$, respectively, for brevity while the dependence on z is still acknowledged. The above equations form a coupled wave equation for $u^{(2)}$ and $v^{(2)}$ forced by $A(\xi, z)$ and $B(\xi, z)$. In principle, $u^{(2)}$ can be eliminated from (D.2) and the resulting second-order differential equation can be solved for $v^{(2)}$, and vice versa. However, we found it more manageable to solve as a system of two coupled equations, by finding particular integrals for each of the forcing terms on the right-hand-side. Ultimately, the solution for $u^{(2)}$ and $v^{(2)}$ are,

$$\begin{aligned} v^{(2)} = & - \left[N \left(n + \frac{y}{h} \right) - N \left(n - \frac{y}{h} \right) \right] - y \left[\frac{\partial B}{\partial z} \left(n + \frac{y}{h} \right) + \frac{\partial B}{\partial z} \left(n - \frac{y}{h} \right) \right] \\ & + \frac{dh/dz}{h^2} y \left[A \left(n + \frac{y}{h} \right) + A \left(n - \frac{y}{h} \right) \right] + y \frac{1}{2} \frac{dp^{(0)}}{dz} \left[B \left(n + \frac{y}{h} \right) + B \left(n - \frac{y}{h} \right) \right] \\ & + \frac{1}{2} y^2 \left(\frac{1}{h} \frac{dp^{(0)}}{dz} - \frac{dh/dz}{h^2} \right) \left[-B' \left(n + \frac{y}{h} \right) + B' \left(n - \frac{y}{h} \right) \right] \\ & - \frac{y}{h} \left[B' \left(n + \frac{y}{h} \right) A \left(n + \frac{y}{h} \right) + B' \left(n - \frac{y}{h} \right) A \left(n - \frac{y}{h} \right) \right] \\ & - \frac{1}{2} \left[B \left(n + \frac{y}{h} \right) A \left(n - \frac{y}{h} \right) + B' \left(n + \frac{y}{h} \right) A \left(n - \frac{y}{h} \right) \right] \\ & + \frac{1}{2} \left[B \left(n - \frac{y}{h} \right) A \left(n + \frac{y}{h} \right) + B' \left(n - \frac{y}{h} \right) A \left(n + \frac{y}{h} \right) \right], \end{aligned} \quad (\text{D.3})$$

$$\begin{aligned}
u^{(2)} = & \left[N\left(n + \frac{y}{h}\right) + N\left(n - \frac{y}{h}\right) \right] + y \left[\frac{\partial B}{\partial z}\left(n + \frac{y}{h}\right) - \frac{\partial B}{\partial z}\left(n - \frac{y}{h}\right) \right] \\
& - \frac{dh/dz}{h^2} y \left[A\left(n + \frac{y}{h}\right) - A\left(n - \frac{y}{h}\right) \right] + y \frac{1}{2} \frac{dp^{(0)}}{dz} \left[B\left(n + \frac{y}{h}\right) - B\left(n - \frac{y}{h}\right) \right] \\
& + \frac{1}{2} y^2 \left(\frac{1}{h} \frac{dp^{(0)}}{dz} - \frac{dh/dz}{h^2} \right) \left[B'\left(n + \frac{y}{h}\right) + B'\left(n - \frac{y}{h}\right) \right] \\
& + \frac{y}{h} \left[B'\left(n + \frac{y}{h}\right) A\left(n + \frac{y}{h}\right) - B'\left(n - \frac{y}{h}\right) A\left(n - \frac{y}{h}\right) \right] \\
& - \frac{1}{2} \left[B\left(n + \frac{y}{h}\right) A\left(n - \frac{y}{h}\right) - B'\left(n + \frac{y}{h}\right) A^\wedge\left(n - \frac{y}{h}\right) \right] \\
& - \frac{1}{2} \left[B\left(n - \frac{y}{h}\right) A\left(n + \frac{y}{h}\right) - B'\left(n - \frac{y}{h}\right) A^\wedge\left(n + \frac{y}{h}\right) \right] \\
& - \frac{1}{2} y^2 \left(\frac{h(d^2h/dz^2) - 2(dh/dz)^2}{h^3} + 2 \frac{dh/dz}{h^2} \frac{dp^{(0)}}{dz} \right) \\
& - \frac{dh/dz}{h} \left[A^\wedge\left(n + \frac{y}{h}\right) + A^\wedge\left(n - \frac{y}{h}\right) \right] - \frac{h}{2} \frac{dp^{(0)}}{dz} \left[B^\wedge\left(n + \frac{y}{h}\right) + B^\wedge\left(n - \frac{y}{h}\right) \right] \\
& + \left[\left(B'\left(n + \frac{y}{h}\right) A\left(n + \frac{y}{h}\right) \right)^\wedge + \left(B'\left(n - \frac{y}{h}\right) A\left(n - \frac{y}{h}\right) \right)^\wedge \right].
\end{aligned} \tag{D.4}$$

where the term $- [N(n + (y/h)) - N(n - (y/h))]$ represents the complementary solution, which is an as-yet-unknown wave, and B^\wedge is the integral of A such that $B^{\wedge'} = B$.

Replacing $v^{(2)}$ into the boundary condition (40) at the second order, $v^{(2)} = (dh/dz)u^{(1)}$, results in

$$\begin{aligned}
\frac{dh}{dz} \left(B(n+1) + B(n-1) \right) = & - \left(N(n+1) - N(n-1) \right) - h \left(\frac{\partial B(n+1)}{\partial z} + \frac{\partial B(n-1)}{\partial z} \right) \\
& + \frac{dh/dz}{h} \left(A(n+1) + A(n-1) \right) + \frac{h}{2} \left(\frac{dp^{(0)}}{dz} \right) \left(B(n+1) + B(n-1) \right) \\
& + \frac{1}{2} h^2 \left(\frac{1}{h} \frac{dp^{(0)}}{dz} - \frac{dh/dz}{h^2} \right) \left(-B'(n+1) + B'(n-1) \right) \\
& - \left(B'(n+1)A(n+1) + B'(n-1)A(n-1) \right) \\
& - \frac{1}{2} \left(B(n+1)A(n-1) + B'(n+1)A^\wedge(n-1) \right) \\
& + \frac{1}{2} \left(B(n-1)A(n+1) + B'(n-1)A^\wedge(n+1) \right).
\end{aligned} \tag{D.5}$$

This equation can be extensively simplified on the surface utilising the periodicity of functions A and B , using equations (28) and (47), to obtain

$$\begin{aligned}
\frac{\partial B(n+1, z)}{\partial z} - \frac{dh/dz}{h^2} A(n+1, z) - \left(\frac{1}{2} \frac{dp^{(0)}}{dz} - \frac{dh/dz}{h} \right) B(n+1, z) \\
+ \frac{1}{h} B'(n+1, z) A(n+1, z) = -\frac{1}{h} (N(n+1, z) - N(n-1, z)).
\end{aligned} \tag{D.6}$$

Setting the right hand side to zero to avoid a secularity condition and N growing as a function of n results in the expressions (50) quoted in Section 3.2.3.

E Advection equation

In this appendix, we rearrange equation (51), given as

$$\frac{\partial}{\partial z} \left(\frac{B(\xi, z)}{(\alpha_2/h)} \right) + \frac{A(\xi, z)}{h} \frac{\partial}{\partial \xi} \left(\frac{B(\xi, z)}{(\alpha_2/h)} \right) - \frac{dh/dz}{\alpha_2 h} A(\xi, z) = 0, \tag{E.1}$$

to include the excitation term within the derivatives, which makes it more convenient to solve. Moreover, if the advection speed is the same as Burger's equation for the stresses (36b), both equations share the same characteristics, again aiding numerical solution. This is the aim of the present appendix.

We start transforming equation (E.1) by multiplying it by h^2/α_1 , giving

$$\frac{h^2}{\alpha_1} \frac{\partial}{\partial z} \left(\frac{B}{(\alpha_2/h)} \right) + \omega \frac{\partial}{\partial \xi} \left(\frac{B}{(\alpha_2/h)} \right) - \frac{dh/dz}{\alpha_2} \omega = 0. \quad (\text{E.2})$$

To remove the excitation term, we look at the multiple of ω which solves equation (E.2). This factor is called $Q(z)$. In this case, we can write,

$$\frac{h^2}{\alpha_1} \frac{\partial}{\partial z} (Q\omega) + \omega \frac{\partial}{\partial \xi} (Q\omega) - \frac{dh/dz}{\alpha_2} \omega = \frac{h^2}{\alpha_1} \omega \frac{dQ}{dz} + Q \left[\frac{h^2}{\alpha_1} \frac{\partial \omega}{\partial z} + \frac{1}{2} \frac{\partial}{\partial \xi} (\omega^2) \right] - \frac{dh/dz}{\alpha_2} \omega = 0. \quad (\text{E.3})$$

The term in the bracket is zero according to Burger's equation (36b). The remaining terms find $Q(z)$ as

$$\frac{h^2}{\alpha_1(z)} \frac{dQ}{dz} = \frac{dh/dz}{\alpha_2(z)} \quad \Rightarrow \quad Q(z) = \int^z \frac{\alpha_1(\bar{z})}{\alpha_2(\bar{z})} \frac{dh(\bar{z})/d(\bar{z})}{h(\bar{z})^2} d\bar{z}. \quad (\text{E.4})$$

Subtracting equation (E.2) and (E.4) results in

$$\frac{h^2}{\alpha_1} \frac{\partial}{\partial z} \left(\frac{B(\xi, z)}{(\alpha_2/h)} - Q(z)\omega(\xi, z) \right) + \omega(\xi, z) \frac{\partial}{\partial \xi} \left(\frac{B(\xi, z)}{(\alpha_2/h)} - Q(z)\omega(\xi, z) \right) = 0. \quad (\text{E.5})$$

With the same change of domain as (36b), we finally have,

$$\frac{\partial}{\partial T} \left(\frac{B}{(\alpha_2/h)} - Q\omega \right) + \omega \frac{\partial}{\partial \xi} \left(\frac{B}{(\alpha_2/h)} - Q\omega \right) = 0, \quad (\text{E.6})$$

which is the expression given in equation (52).

References

- [1] Allwood and Cullen, (2012). *Sustainable Materials: With Both Eyes Open*. UIT Cambridge. ISBN 978-1906860059.
- [2] Lenard, (2014). *Primer on flat rolling*. Newnes, 2nd edition. doi: 10.1016/C2012-0-06474-5. ISBN 978-0-08-099418-5.
- [3] Allwood, Duncan, Cao, Groche, Hirt, Kinsey, Kuboki, Liewald, Sterzing, and Tekkaya, (2016). "Closed-loop control of product properties in metal forming". *CIRP Ann.*, **65**(2) 573–596. doi: 10.1016/j.cirp.2016.06.002.
- [4] Idzik, Krämer, Hirt, and Lohmar, (2024). "Coupling of an analytical rolling model and reinforcement learning to design pass schedules: towards properties controlled hot rolling". *J. Intell. Manuf.*, **35**(4) 1469–1490. doi: 10.1007/s10845-023-02115-2.
- [5] Trzepieciniski and Lemu, (2017). "Effect of computational parameters on springback prediction by numerical simulation". *Metals*, **7**(9) 380. doi: 10.3390/met7090380.
- [6] Prabhu, Kulkarni, and Sharma, (2020). "Multi-response optimization of the turn-assisted deep cold rolling process parameters for enhanced surface characteristics and residual stress of AISI 4140 steel shafts". *J. Mater. Res. Technol.*, **9**(5) 11402–11423. doi: 10.1016/j.jmrt.2020.08.025.
- [7] Kumar, Rath, and Kumar, (2021). "Simulation of plate rolling process using finite element method". *Mater. Today Proc.*, **42** 650–659. doi: 10.1016/j.matpr.2020.11.050.
- [8] Flanagan, O'Connor, Erfanian, Music, Brambley, and O'Kiely. "Careful finite element simulations of cold rolling with accurate through-thickness resolution and prediction of residual stress". submitted to *Int. J. Mech. Sci.*, (2024).
- [9] Decroos, Sidor, and Seefeldt, (2014). "A new analytical approach for the velocity field in rolling processes and its application in through-thickness texture prediction". *Metall. and Mater. Trans. A*, **45** 948–961. doi: 10.1007/s11661-013-2021-3.
- [10] von Kármán, (1925). "On the theory of rolling". *Z. Angew. Math. Mech*, **5** 139–141. doi: 10.1002/zamm.19250050213. In German.
- [11] Siebel and Pomp, (1927). "Die ermittlung der formänderungsfestigkeit von metallen durch den stauchversuch". *Mitteilungen aus dem Kaiser Wilhelm Institut für Eisenforschung*, **9**(8) 157.
- [12] Roychoudhuri and Lenard, (1984). "A mathematical model of cold rolling-experimental substantiation". In *Proceedings of the 1st International Conference on Technology of Plasticity, Tokyo, Japan*, pages 1138–1143.

- [13] Fleck, Johnson, Mear, and Zhang, (1992). “Cold rolling of foil”. *Proc. Inst. Mech. Eng. B*, **206**(2) 119–131. doi: 10.1243/PIME_PROC_1992_206_064_02.
- [14] Orowan, (1943). “The calculation of roll pressure in hot and cold flat rolling”. *Proc. Inst. Mech. Eng.*, **150**(1) 140–167. doi: 10.1243/PIME_PROC_1943_150_025_02.
- [15] Nadai, (1931). *Plasticity*. McGraw-Hill.
- [16] Orowan and Pascoe, (1946). “First report of the rolling-mill research sub-committee”. Technical Report 34, Iron and Steel Institute.
- [17] Bland and Ford, (1948). “The calculation of roll force and torque in cold strip rolling with tensions”. *Proc. Inst. Mech. Eng.*, **159**(1) 144–163. doi: 10.1243/PIME_PROC_1948_159_015_0.
- [18] Bland and Ford, (1952). “Cold rolling with strip tension, part III: An approximate treatment of the elastic compression of the strip in rolling mills”. *J. Iron Steel Inst.*, **171**(3) 245–249.
- [19] MacGregor and Palme, (1959). “The distribution of contact pressures in the rolling of metals”. *J. Basic Eng.*, **81**(4) 669–679. doi: 10.1115/1.4008589.
- [20] Firbank and Lancaster, (1965). “A suggested slip-line field for cold rolling with slipping friction”. *Int. J. Mech. Sci.*, **7**(12) 847–852. doi: 10.1016/0020-7403(65)90037-8.
- [21] Al-Salehi, Firbank, and Lancaster, (1973). “An experimental determination of the roll pressure distributions in cold rolling”. *Int. J. Mech. Sci.*, **15**(9) 693–710. doi: 10.1016/0020-7403(73)90049-0.
- [22] Yarita, Mallett, and Lee, (1985). “Stress and deformation analysis of plane-strain rolling process”. *Steel Res.*, **56**(5) 255–259. doi: doi.org/10.1002/srin.198500631.
- [23] Prakash, Dixit, and Lal, (1995). “Steady-state plane-strain cold rolling of a strain-hardening material”. *J. Mater. Process. Technol.*, **52**(2-4) 338–358. doi: 10.1016/0924-0136(94)01728-J.
- [24] Montmitonnet, (2006). “Hot and cold strip rolling processes”. *Comput. Methods Appl. Mech. Eng.*, **195**(48-49) 6604–6625. doi: 10.1016/j.cma.2005.10.014.
- [25] Flanagan, O’Kiely, O’Connor, Erfanian, and Brambley, (2023). “New discoveries in cold rolling: understanding stress distribution and parameter dependence for faster, more accurate models”. In *International Conference on the Technology of Plasticity*, pages 211–222. Springer. doi: 10.1007/978-3-031-41023-9_22.
- [26] Minton, Cawthorn, and Brambley, (2016). “Asymptotic analysis of asymmetric thin sheet rolling”. *Int. J. Mech. Sci.*, **113** 36–48. doi: 10.1016/j.ijmecsci.2016.03.024.
- [27] Smet and Johnson, (1989). “An asymptotic analysis of cold sheet rolling”. *J. Appl. Mech.* doi: 10.1115/1.3176062.
- [28] Domanti and McElwain, (1995). “Two-dimensional plane strain rolling: an asymptotic approach to the estimation of inhomogeneous effects”. *Int. J. Mech. Sci.*, **37**(2) 175–196. doi: 10.1016/0020-7403(94)00053-M.
- [29] Johnson and Smelser, (1992). “An asymptotic formulation of shear effects in two dimensional rolling”. *J. Mater. Process. Technol.*, **34**(1-4) 311–318. doi: 10.1016/0924-0136(92)90122-9.
- [30] Cawthorn, Minton, and Brambley, (2016). “Asymptotic analysis of cold sandwich rolling”. *Int. J. Mech. Sci.*, **106** 184–193. doi: 10.1016/j.ijmecsci.2015.12.012.
- [31] Minton, (2017). *Mathematical modelling of asymmetrical metal rolling processes*. PhD thesis, University of Cambridge.
- [32] Dassault Systèmes Simulia Corp. *SIMULIA User Assistance 2021 Abaqus*, (2021). <https://www.3ds.com/support/documentation/user-guides>.
- [33] Hinch, (1991). *Perturbation Methods*, chapter 7, pages 116–143. Cambridge. doi: 10.1017/CBO9781139172189.
- [34] Roberts, (2015). *Model Emergent Dynamics in Complex Systems*. SIAM. doi: 10.1137/1.9781611973563. ISBN 9781611973563.
- [35] Valéry Roy, Roberts, and Simpson, (2002). “A lubrication model of coating flows over a curved substrate in space”. *J. Fluid Mech.*, **454**. doi: 10.1017/S0022112001007133.
- [36] Roberts, (1993). “The invariant manifold of beam deformations”. *J. Elast.*, **30** 1–54. doi: 10.1007/BF00041769.
- [37] Brambley and Peake, (2008). “Sound transmission in strongly curved slowly varying cylindrical ducts with flow”. *J. Fluid Mech.*, **596** 387–412. doi: 10.1017/S0022112007009603.
- [38] Cherukuri, Johnson, and Smelser, (1997). “A rate-dependent model for hot-rolling”. *Int. J. Mech. Sci.*, **39**(6) 705–727. doi: 10.1016/S0020-7403(97)81242-8.
- [39] MathWorks Inc. *MATLAB version: 24.1.0.2568132 (R2024a) Update 1*, (2024). <https://www.mathworks.com>.

- [40] Spittel and Spittel, (2009). “Steel symbol/number: DC04/1.0338”. In *Metal Forming Data of Ferrous Alloys — Deformation Behaviour*, pages 162–167. Springer-Verlag.
doi: 10.1007/978-3-540-44760-3_18.
- [41] Johnson, Sowerby, and Venter, (1982). *Plane-strain slip-line fields for metal-deformation processes: a source book and bibliography*. Pergamon. doi: 10.1016/C2013-0-10170-5. ISBN 978-0-08-025452-4.
- [42] Olaogun, Edberg, Lindgren, Oluwole, and Akinlabi, (2019). “Heat transfer in cold rolling process of AA8015 alloy: a case study of 2-D FE simulation of coupled thermo-mechanical modeling”. *Int. J. Adv. Manuf. Technol.*, **100** 2617–2627. doi: 10.1007/s00170-018-2811-2.
- [43] Kazeminezhad and Taheri, (2006). “Calculation of the rolling pressure distribution and force in wire flat rolling process”. *J. Mater. Process. Technol.*, **171**(2) 253–258.
doi: 10.1016/j.jmatprotec.2005.06.070.
- [44] Vallellano, Cabanillas, and Garcia-Lomas, (2008). “Analysis of deformations and stresses in flat rolling of wire”. *J. Mater. Process. Technol.*, **195**(1-3) 63–71.
doi: 10.1016/j.jmatprotec.2007.04.124.
- [45] Erfanian, Brambley, Flanagan, O’Kiely, and O’Connor, (2023). “New models for cold rolling: Generalized slab theory and slip lines for fast predictions without finite elements”. In *International Conference on the Technology of Plasticity*, pages 223–233. doi: 10.1007/978-3-031-41023-9_23.